Petroleum Science 23 (2026) 5334–5358

Contents lists available at ScienceDirect

Petroleum Science

journal homepage: www.keaipublishing.com/en/journals/petroleum-science

Original Paper

Stochastic simulation and finely characterization of heterogeneous reservoirs based on MSGAN and BicycleGAN

Xue-Chao Wu [a], Wen-Yao Fan [b,c,*], Shi-Jie Peng [d], Xin-Hua Xu [a], Feng Deng [e], Xi-Xi Du [a]

[a] School of Artificial Intelligence and Computer Science, Hubei Normal University, Huangshi, 435002, Hubei, China
[b] DER/CERENA, Instituto Superior Técnico, Universidade de Lisboa, 1049-001, Lisboa, Portugal
[c] School of Computer Science, China University of Geosciences, Wuhan, 430074, Hubei, China
[d] Hubei Post and Telecommunications Planning and Design Co., Ltd., Wuhan, 430074, Hubei, China
[e] Hubei Academy of Scientific and Technical Information, Wuhan, 430074, Hubei, China

A R T I C L E I N F O

Article history:
Received 11 November 2025
Received in revised form
19 May 2026
Accepted 5 July 2026
Available online 11 July 2026

Edited by Xiu-Fang Hu

Keywords:
Reservoir modeling
Generative adversarial networks
Heterogeneous geological patterns
Data augmentation
Conditional simulation

A B S T R A C T

Subsurface reservoirs can be constructed based on Generative Adversarial Networks (GANs), but some challenges cannot be overlooked. For example, both prior geological patterns and knowledge are hardly quantified so that GANs cannot be trained without sufficient samples. Meanwhile, the heterogeneous patterns are difficult to characterize, with less consideration of multiple geological constraints, resulting in poor modeling accuracy and reliability. Therefore, we integrated Multi-Stage GAN (MSGAN) and BicycleGAN to finely characterize heterogeneous reservoirs. Specifically, MSGAN can extract and quantify geological patterns based on multiscale representations of pyramid structure. Through concurrent training and parameter inheritance, these simulated prior samples share the same feature space with the Training Image (TI) so that they can support BicycleGAN's training. The bijective consistency between latent codes and output modes is established, and reservoir characterization is achieved through the nonlinear mapping between multiple conditioning data and output modes. Both synthetic cases and field application were introduced to verify the applicability of the proposed modeling framework. During data augmentation based on MSGAN, different simulations preserve a better generation diversity, and the complex geological pattern fitting with multiple geological constraints can be reproduced by BicycleGAN. Each conditional simulation is similar to TI in terms of spatial variability, channel connectivity and spatial structures, significantly reducing modeling uncertainties.

1. Introduction

Nowadays, unconventional resources exploration makes a breakthrough based on advanced techniques (i.e., horizontal drilling, high-precision 3D seismic prediction, etc.), which plays an important role in national economic development and industrial revolution (Liao et al., 2024; Yang et al., 2022). The complex subsurface storage space and physicochemical properties of surrounding rocks provide a solid foundation for the resource accumulation and transportation (Mishra et al., 2022; Yang et al., 2022). Recently, the deep-buried structural reservoir has aroused much attention, but the nonlinear spatial correlation and distribution are more complex, with significant heterogeneity and anisotropy (Hosseinzadeh and Tavakoli, 2024; Madalimov et al., 2025). Meanwhile, with the limited understanding for geological backgrounds and sedimentary evolutions, both reservoir structures and internal physical parameter distributions cannot be characterized accurately. Reservoir modeling can integrate multi-source geological information, with geobody development scale, geometric shape and physical parameter distributions being visualized comprehensively (Cui et al., 2025; Fan et al., 2024a). Therefore, heterogeneous reservoir characterization is crucial for the unconventional resource exploration and assessment (Cui et al., 2025; Madalimov et al., 2025; Wu et al., 2024; Yang et al., 2022).

* Corresponding author.
E-mail address: fanwy_jlu@163.com (W.-Y. Fan).
Peer review under the responsibility of China University of Petroleum (Beijing).

https://doi.org/10.1016/j.petsci.2026.07.009
1995-8226/

Reservoir modeling can be divided into deterministic and stochastic approaches (Cui et al., 2025; Fan et al., 2024a). Among them, deterministic modeling is suitable for the regions with abundant observations and simple geological structures. For the heterogeneous reservoir bodies, however, the spatial resolution is low and the modeling uncertainties cannot be quantified (Caers, 2011; Grana et al., 2021; Khalili and Ahmadi, 2023). Stochastic modeling has a higher spatial resolution and modeling efficiency compared with deterministic ones, and modeling uncertainties are quantified based on multiple equiprobable outputs (Grana et al., 2021; Khalili and Ahmadi, 2023; Li et al., 2021; Sakki et al., 2022). As a typical stochastic simulation approach, the core idea of geostatistical simulation is that regional variables in geological domain are assumed to have a statistical correlation, and distributions of different physical parameters can be reproduced based on random function theories (Fan et al., 2025; Zakeri and Mariethoz, 2021). For example, two-point statistics can characterize geological patterns based on variogram function, with spatial correlation between two points being only considered, which is not suitable for the complex geobody modeling (Abulkhair and Madani, 2022; Li et al., 2015). Multiple-point Statistics (MPS) can overcome these shortcomings, which uses Training Images (TIs) to present regional variables correlation and high-order statistical information so that geobody structure-attribute properties are well reproduced (Levy et al., 2024; Mariethoz and Caers, 2014; Zhou et al., 2024). TIs herein are regarded as the prior models including both real observations and geological knowledge (Mariethoz and Caers, 2014). However, traditional MPS are based on the stationarity assumption, presenting a poor simulation performance under nonstationary scenarios. Some improvements, such as probability fusion based on τ-model (Krishnan, 2008), local neighboring search (Chen et al., 2018) and locally linear embedding (Zhang et al., 2017), were proposed to reproduce the complex geological patterns under nonstationary conditions, but too many parameters need to be predefined manually, which is complicated and less efficient for the large-scale and successive simulation processes.

Geo-modeling can be regarded as a target generation, which can be achieved through deep generative learning. It uses nonlinear neural network to fit high-order statistical distribution of training samples so that realistic outputs are created (Salakhutdinov, 2015). Due to their adversarial learning and better fitting abilities, Generative Adversarial Networks (GANs) show great potential in terms of complex reservoir modeling. The target of the Generator (G) is to output results that are similar to the training samples, while the Discriminator (D) can distinguish whether the input data derives from training samples (marked as True) or from G (marked as False). Through iteratively training, the “Nash Equilibrium” is reached between G and D, that is, the output patterns are similar to the training samples, and D cannot distinguish where the input data derives from (Aggarwal et al., 2021; Creswell et al., 2018; Goodfellow et al., 2016), then the pretrained G can be loaded repeatedly to realize the target generation. The variations of GANs are widely used in the reservoir modeling fields. For instance, for the heterogeneous pore media reconstruction, Zhang and Zhang (2025) integrated Transformer (Vaswani et al., 2017) into GANs to improve the abilities of contextual information extraction and long-term dependency modeling, achieving the multiscale and diverse characterization of pore structures. Xu et al. (2025) proposed a multistage and multiscale simulation strategy based on GANs. With the integration of U-Net structure, multiscale discrimination and feature fusion blocks, the reconstructed equiaxed pore systems show a clear geometric shape and better connectivity. Based on focused-ion-beam scanning electron microscope (FIB-SEM), Liang et al. (2024) proposed a stepwise 3D super-resolution reconstruction of shale pore structures. It addresses the problems of inconsistency between horizontal and vertical resolutions to enhance the reconstruction clarity, providing foundations for evaluating pore sizes distribution and connectivity. For better constructing subsurface sedimentary systems, the SA-RelayGANs based on two-stage simulations were proposed by Cui et al. (2024). In the first stage, the heterogeneous subsurface structure was created to constrain the property prediction in the second stage, presenting a better modeling capability for the nonstationary delta construction. Based on single TI, Zhou and Shi (2025) used multiscale symmetrical GANs to perform unsupervised learning so that oversimplification of sedimentary facies distribution and stronger dependency of prior knowledge can be better solved. Furthermore, GANs are also successfully applied in the reservoir numerical simulations. A GAN-based inversion algorithm was proposed by Xie et al. (2022) to integrate both geological pattern and prior knowledge. Then, Metropolis Markov Chain Monte Carlo (MCMC) was introduced to select the optimal geomodels so that inversion accuracy and modeling qualities are improved. For accelerating the history matching and optimization efficiencies, Wang et al. (2024) proposed a dynamic prediction model based on a variety of view deep convolutional encoder-decoder network, which can consider the effects of reservoir heterogeneity and time-varying well impacts simultaneously, thereby improving the training efficiency and prediction accuracy.

However, some challenges still exist for the current GANs-based modeling techniques: (1) Training process of GANs is always supported by abundant samples, for real application, however, the number of prior samples are limited, with corresponding prior geological knowledge being hardly quantified; (2) Deep-buried reservoir units are subjected to multistage sedimentary evolutions, with significant heterogeneity and complex geometric shape, and the internal physical parameters are randomly distributed. It is difficult for the traditional GANs to finely extract the reservoir patterns, and the output diversity is too poor to quantify the modeling uncertainties; (3) During reservoir exploration, the sparse distributed observations might be regarded as a random noise by GANs so that the reconstructed geo-models cannot fit with the weak geological constraints. Meanwhile, it is difficult for GANs to define the nonlinear mapping correlation between multisource conditioning data and output modes. Therefore, it is necessary to quantify geological patterns and knowledge to create abundant and realistic prior training samples. Then, based on multisource conditioning data, we need to improve the structure and optimization process of GANs to achieve the reservoir conditional simulation accurately.

In this paper, we integrated Multi-Stage GAN (MSGAN) and BicycleGAN to achieve 3D reservoir conditional simulation. MSGAN herein is a kind of stochastic generating framework based on small samples, which can capture global patterns and detailed information of TI under small-scale and large-scale based on multiscale representations of pyramid structure, thereby generating diverse and realistic geological prior samples. Since the generated prior geological information shares the same feature space with TI, we used the BicycleGAN to perform reservoir conditional simulation. Compared with some GAN's variants (i.e., Progressive Growing GAN (PGGAN) and Style-based GAN), BicycleGAN is a kind of light-weighted multi-modal image-to-image translation framework, which uses the bijective consistency between latent space and output modes to extract and quantify the training sample high-order statistics. Meanwhile, the nonlinear mapping between input conditioning data and output reservoir patterns is defined so that the reconstructed models fit with geological constraints. Though PGGAN and StyleGAN can create high-resolution images, there are still some challenges during reservoir conditional simulation (i.e., facies mismatch at well locations, huge computing overburden and training stability). Two synthetic TIs were introduced to verify the data augmentation quality of MSGAN and simulation performance of BicycleGAN respectively. Then, the hybrid framework was discussed in different aspects (i.e., parameter sensitivity analysis and comparative studies) and finally introduced into a real case application to further verify the modeling applicability.

2. Methodologies

Fig. 1 illustrates the proposed modeling framework. Firstly, we used the MSGAN to perform data augmentation based on prior geo-models (TIs), then the conditioning dataset was defined for each prior sample, which were used for training BicycleGAN to realize the geobody conditional simulation.

2.1. Data augmentation based on MSGAN

2.1.1. Network structure and training optimization of MSGAN

A pyramid structure was introduced in MSGAN (Fig. 2) to downsample TI (with length, width and height marked as L, W and H) into different sizes. Specifically, assuming there are n training stages, $y_i=(L_i,W_i,H_i)(i=1,\dots,n-1)$ refers to the target downsampling sizes in the i th training stage. If the size at n th stage is predefined as $y_n=(L_n,W_n,H_n)$ (where $L_n\le L$, $W_n\le W$ and $H_n\le H$), then in the remaining training stages, the sizes of TI after downsampling are calculated as:

$$y_i=y_n\times m^{((n-1)/\log n)\cdot\log(n-i)+1},\ i=1,\dots,n-1, \tag{1}$$

$$m=(\min(L_1,H_1,W_1)/\min(L\cdot\delta,W\cdot\delta,H\cdot\delta))^{1/(n-1)}, \tag{2}$$

$$\delta=\min(\max(L_n,W_n,H_n)\,/\,\max(L,W,H),1), \tag{3}$$

where min(*) and max(*) denotes the minimizing and maximizing functions, m and δ are the scale factors reflecting the increasing trend of downsampling sizes from small-scale to large-scale. Note that y_n controls the output size in the final stage (equal to (L,H,W) by default), and the simulation performance is impacted by n. For 3D cases, n can be set within 5–7 to avoid mode collapse (i.e., when n is too small) or overfitting issues (i.e., when n is too large). Then, m and δ should be controlled within 0.6–0.85 to keep the geological pattern fidelity. If the scale factors are too low, the statistical

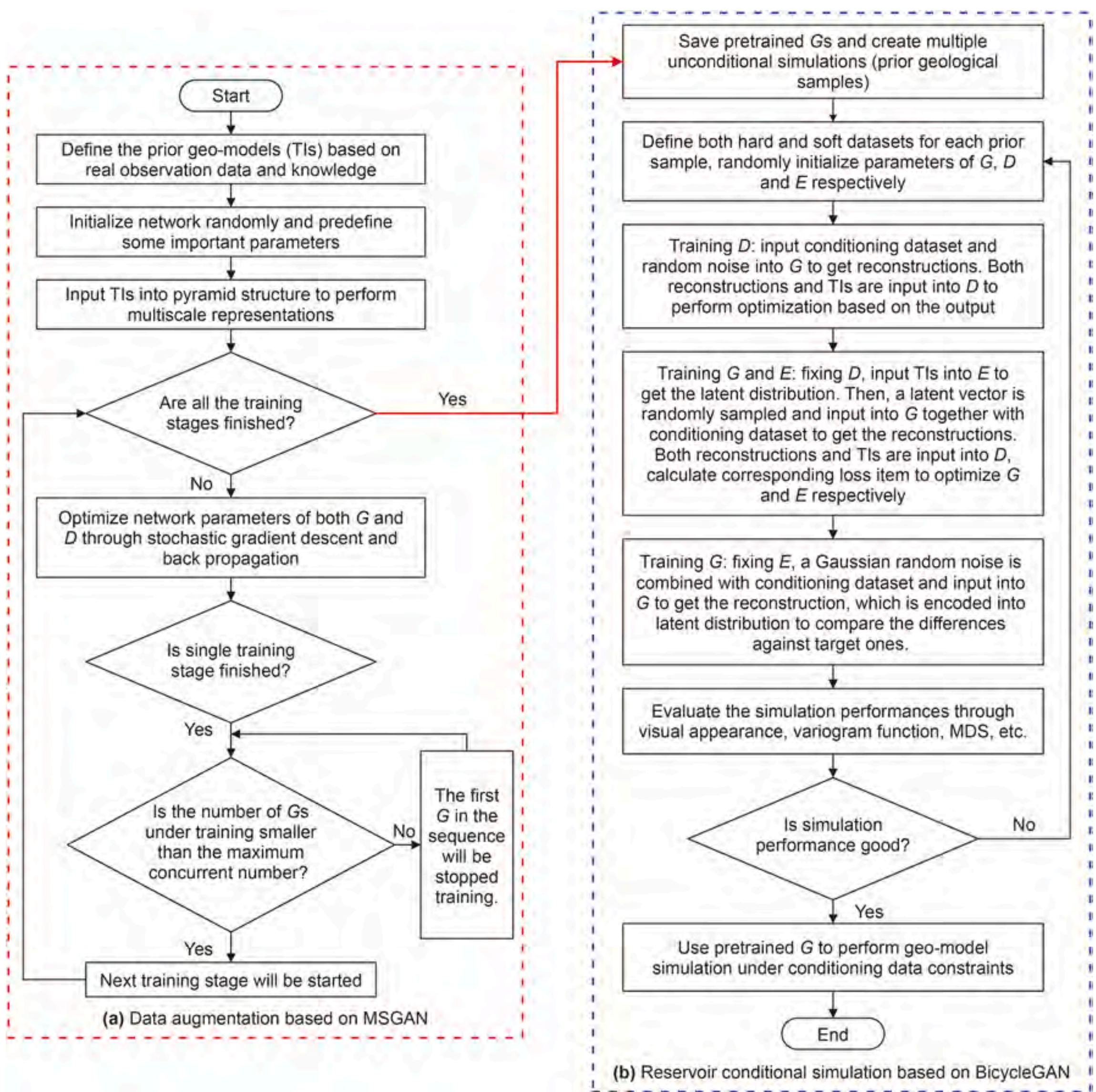

Fig. 1. Experimental flowchart illustrating the data augmentation based on MSGAN **(a)** and reservoir conditional simulation based on BicycleGAN **(b)**.

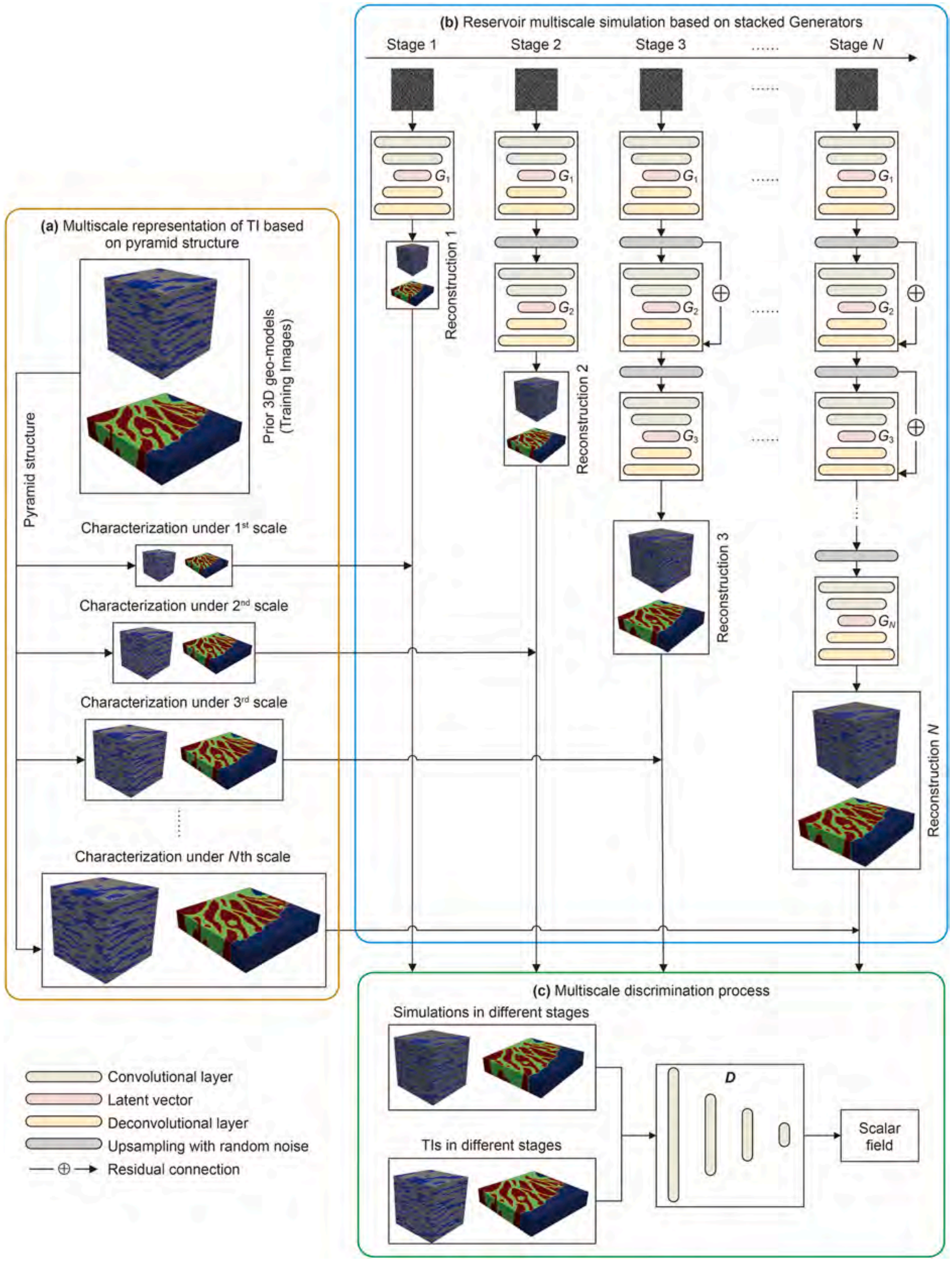

Fig. 2. Network structure and training process of MSGAN.

differences in adjacent scales are relatively large, resulting in poor performance in multi-scale geological pattern extraction and channel connectivity. In contrast, a huge computing consumption and redundant training might occur under relatively high scale factors. The range of these variables are determined through trial-and-error. Therefore, within reasonable value of n, m, δ and y_n, these downsampled geological patterns (i.e., channel connectivity, nonstationary pattern and nonlinear boundaries) can be smoothly transmitted under different scales, with global geological information (i.e., channel distribution) being presented in the coarse-scale TI. With scale increasing, the detailed features (i.e., channel boundaries and geometric shapes) are gradually presented so that the receptive field in MSGAN can extract multiple geological patterns under different scales.

The TI sets $\{TI_1, TI_2, \ldots, TI_n\}$ through downsampling of pyramid structure are used for training MSGAN. In the first training stage, there is only one Generator G_1 referring to the U-Net framework along with multiple deep convolutional units (Ronneberger et al., 2015). Then, a random noise z_1 is randomly sampled from the Gaussian distribution and input into G_1 to get the current reconstruction rec_1. After that, both rec_1 and TI_1 are input into D_1 to distinguish the Ture/False probabilities. D_1 herein refers to the PatchGAN-based form, which can perform discrimination task through outputting scalar matrices (Isola et al., 2017). After optimizing G_1 and D_1 through stochastic gradient descent and back propagation, in the second training stage, the output of G_1 is upsampled and combined with z_2, which is input into an additional G_2 to get the current reconstruction rec_2. Both rec_2 and TI_2 are input into D_2 to perform discrimination process, with G_2 and D_2 being optimized iteratively in the same way. By repeating such process, until the n th training stage, there are n Generators $\{G_1, G_2, \ldots, G_n\}$ connected with upsampling operators so that the final output keeps the same size as the original TI.

Multiple Gs in MSGAN should be optimized to improve the simulation quality. As the training stages increase, a higher computing consumption may occur if all the Gs are optimized simultaneously. In contrast, the parameter values will deviate from the global optimum if only one G is optimized, resulting in a poor simulation performance. Therefore, to balance the correlation between simulation performance and computing efficiency, three

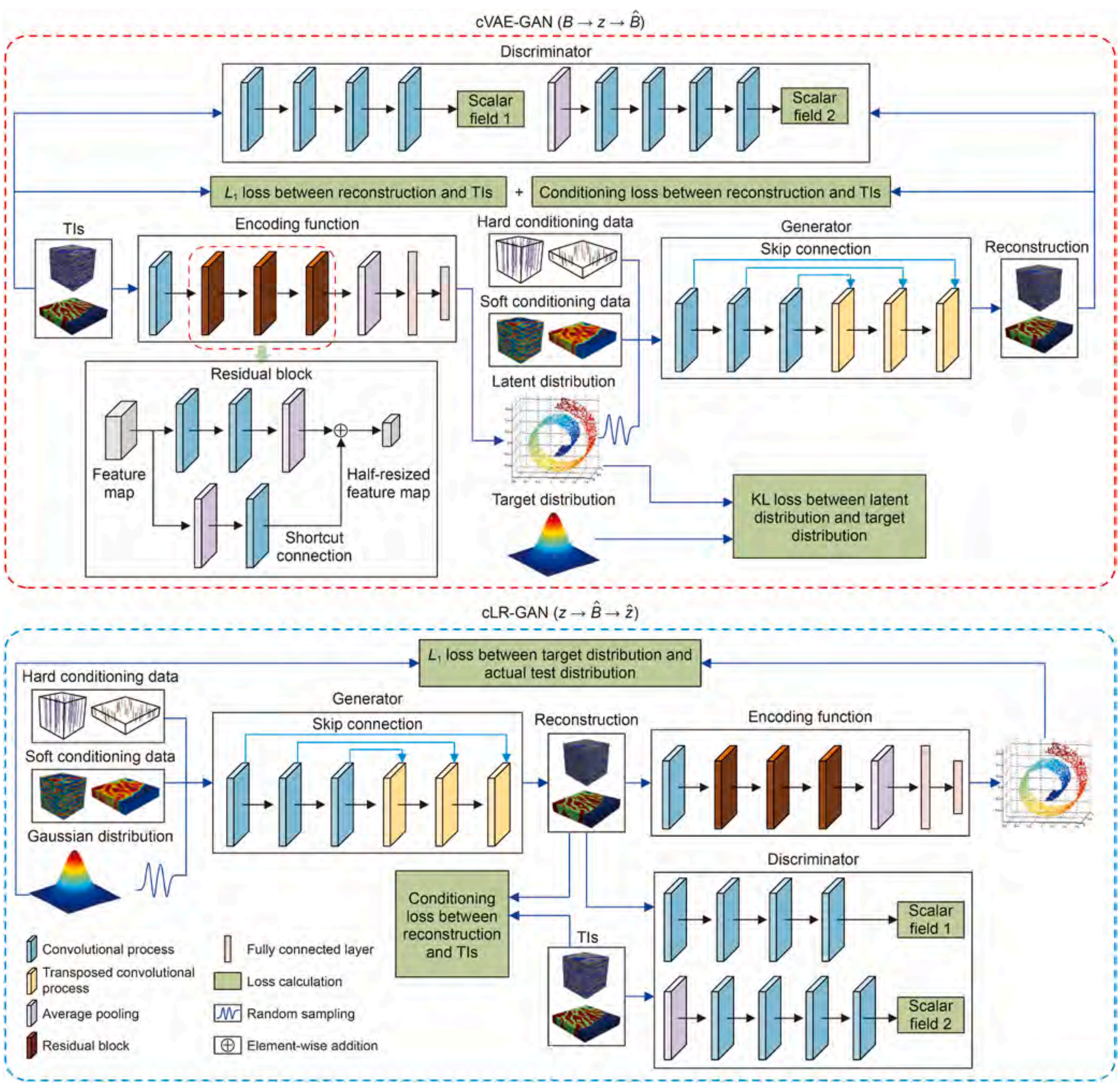

Fig. 3. Schematic diagram of BicycleGAN illustrating network architecture and training process.

strategies are introduced to enable MSGAN to create realistic and diverse prior geological patterns:

(1) Parameter inheritance: two adjacent *G*s in MSGAN are connected with the upsampling operator, and the corresponding output geological patterns are similar to each other. Therefore, it can be inferred that the network parameters for two adjacent *G*s are also highly correlated. Therefore, when the previous *G* has finished training, the pretrained parameters can be directly assigned to the *G* at the current training stage rather than being randomly initialized. The parameter inheritance accelerates the convergence of MSGAN so that the optimum values can be transmitted across different training stages, avoiding mode collapse issues.
(2) Concurrent training pattern: the concurrent training pattern is introduced in MSGAN to optimize the whole training process. Specifically, the maximum concurrent training number $C_{\max}$ is predefined to control the number of *G*s (n_{G}) that needs to be trained. With the training stages increasing, n_{G} are gradually included in the training sequence. When $n_{\mathrm{G}} \le C_{\max}$, all the *G*s in the training sequence are optimized simultaneously. However, when $n_{\mathrm{G}} > C_{\max}$, the $(n_{\mathrm{G}} - C_{\max})$th *G* has already been trained many times, which is fixed and popped out from the training sequence to reduce the GPU computing burden, while the remaining *G*s continue to be trained. Meanwhile, different learning rates are assigned for n_{G} as follows:

$$\theta_i = \theta_n \cdot \lambda^{n-i},\ i \in \{0, 1, \ldots, n\}, \tag{4}$$

where θ_n is the predefined learning rate in the n th training stage, λ is the scale factor set to 0.1 by default. From Eq. (4), a large learning rate is assigned to the *G* that are newly introduced in the training sequence, while a smaller learning rate is assigned to the *G*s that have been trained at least one time. Based on the concurrent training pattern and dynamic fine-tuning of learning rate, multiple *G*s in different training stages are fully optimized.

(3) Residual connection: for the stacked Generator sequence $\{G_1, G_2, \ldots, G_n\}$, from the third training stage, a residual connection was introduced between G_k and G_{k+1}, where $1 \le k \le n-1$. Specifically, the output of G_k is upsampled and combined with that of G_{k+1} through a shortcut connection,

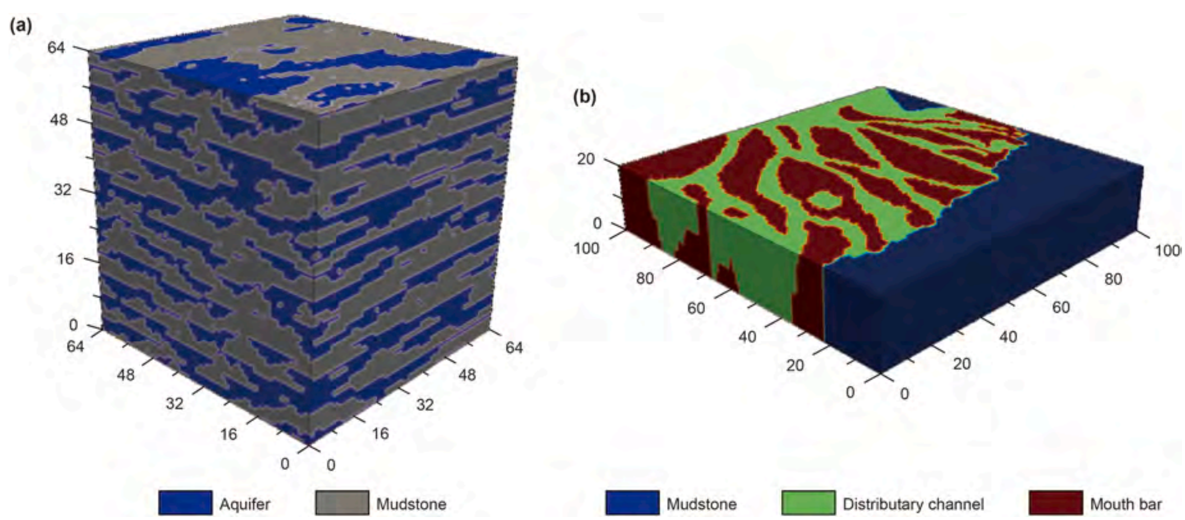

Fig. 4. 3D reservoir TIs: **(a)** aquifer structural model; **(b)** sedimentary delta model.

Table 1
Parameter settings during training MSGAN and BicycleGAN.

Process	Parameters	Functions	Aquifer structural model	Sedimentary delta model
Data augmentation based on MSGAN	T_{MSGAN}	Training iteration times of MSGAN	500	400
	min_size	The size of the generated image at initial training stage	10×10×10	10×10×10
	$\mathrm{num}_{\mathrm{train}}$	Total training stages	5	5
	θ_{MSGAN}	Learning rate of MSGAN	0.0002	0.0001
	$C_{\max}$	Maximum concurrent training number	2	3
	α_{gp}	Weight coefficient of $\mathcal{L}_{\mathrm{gp}}$	0.1	0.1
	α_{rec}	Weight coefficient of $\mathcal{L}_{\mathrm{rec}}$	10	10
Conditional simulation based on BicycleGAN	$T_{\mathrm{BicycleGAN}}$	Training iteration times of BicycleGAN	50	30
	batch_size	The mini-batch samples randomly selected from the dataset	2	2
	$z_{\dim}$	Noise dimension	8	8
	λ_{KL}	Weight coefficient of $\mathcal{L}_{\mathrm{KL}}$	0.01	0.02
	λ_{L_1}	Weight coefficient of $\mathcal{L}_1^{\mathrm{VAE}}$	10	10
	$\lambda_{\mathrm{latent}}$	Weight coefficient of $\mathcal{L}_1^{\mathrm{latent}}$	0.5	0.5
	λ_{con}	Weight coefficient of $\mathcal{L}_{\mathrm{con}}$	1	1
	$\theta_{\mathrm{BicycleGAN}}$	Learning rate of BicycleGAN	0.0002	0.0002

Table 2
Training time consumption and GPU memory usages based on two networks under two different scenarios.

Process	Training time consumption, s		GPU memory usage, %	
	Aquifer structural model	Sedimentary delta model	Aquifer structural model	Sedimentary delta model
Data augmentation based on MSGAN	2374.95	1785.64	92.67	68.75
Conditional simulation based on BicycleGAN	1257.65	1186.49	35.65	32.78

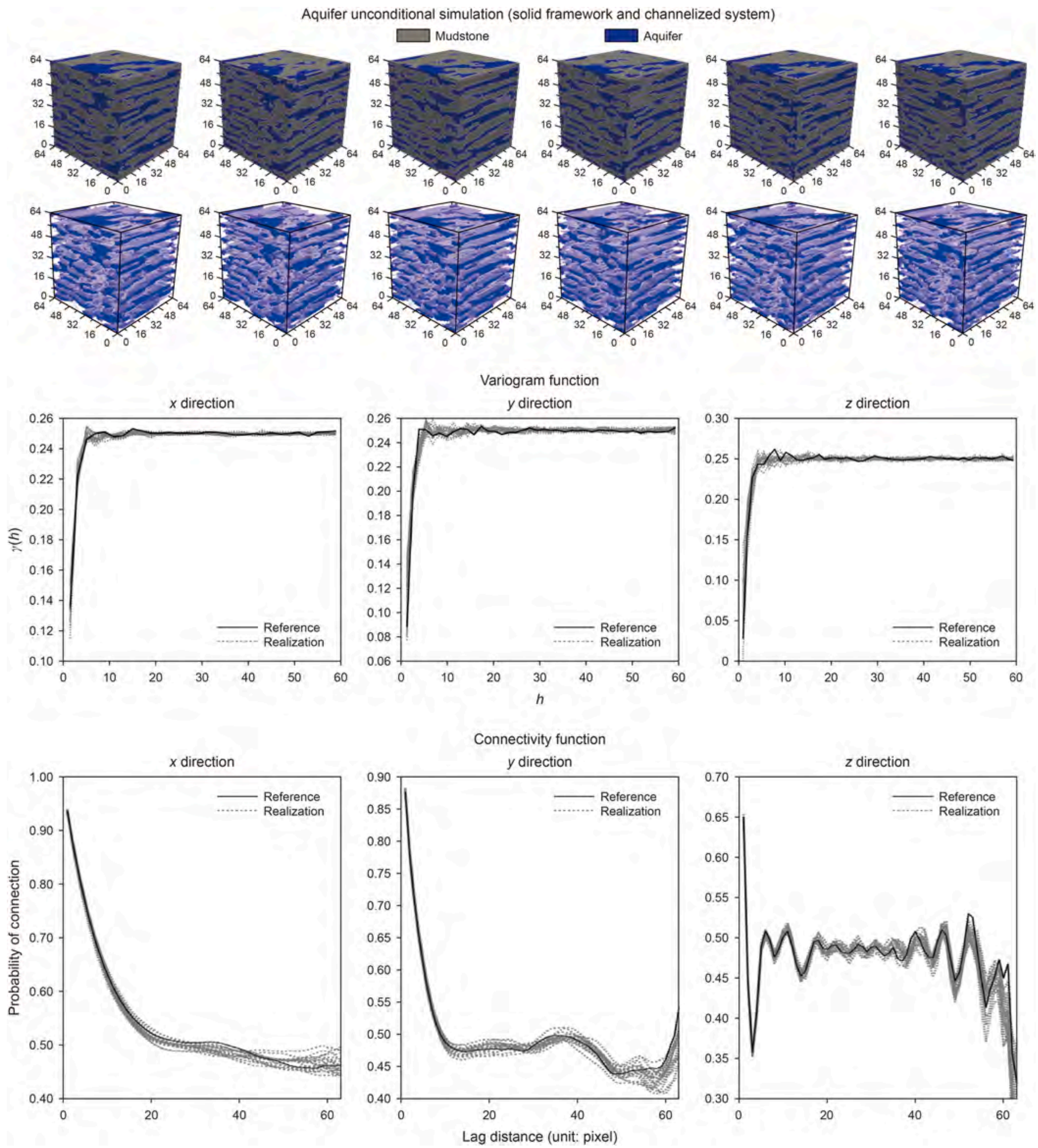

Fig. 5. Unconditional simulation of aquifer structural model based on MSGAN and quantitative evaluations during batch simulation.

thereby a “mixed” feature map is created and used as the input of G_{k+2}. The identity mapping between input and output can be learned based on residual connection to further improve the characterization diversity of geological patterns.

2.1.2. Loss function of MSGAN

A joint loss function was defined in MSGAN to optimize G and D in different training stages:

$$\mathcal{L}_{\mathrm{MSGAN}}(G_i,D_i)=\min_{G_i}\max_{D_i}\alpha_{\mathrm{adv}}\mathcal{L}_{\mathrm{adv}}(G_i,D_i)+\alpha_{\mathrm{rec}}\mathcal{L}_{\mathrm{rec}}(G_i),\quad i\in\{0,1,\ldots,n\}, \tag{5}$$

where $\mathcal{L}_{\mathrm{adv}}(G_i,D_i)$ and $\mathcal{L}_{\mathrm{rec}}(G_i)$ denote the adversarial loss and reconstruction loss respectively, with different coefficient terms α_{adv} and α_{rec} used to balance the weights. α_{adv} makes MSGAN generate the natural geological prior during adversarial learning, which is set to 1 by default. However, α_{rec} should be set within a reasonable range, otherwise, the poor generation ability or overfitting issue may occur if α_{rec} is too small or too large. $\mathcal{L}_{\mathrm{adv}}(G_i,D_i)$ is defined as:

$$\begin{cases}\mathcal{L}_{\mathrm{adv}}(G_i,D_i)=\mathbb{E}_{\tilde{x}_i\sim P_{\mathrm{g}}}\left[D\left(\tilde{x}_i\right)\right]-\mathbb{E}_{x_i\sim P_{\mathrm{r}}}[D(x_i)]+\alpha_{\mathrm{gp}}\mathcal{L}_{\mathrm{gp}}\\ \mathcal{L}_{\mathrm{gp}}=\mathbb{E}_{\hat{x}\sim P_{\hat{x}}}\left[\left(\|\nabla_{\hat{x}}(D(\hat{x}))\|_2-1\right)^2\right]\\ \tilde{x}_i=\begin{cases}G(z_i),\ i=1,\\ G\left(z_i,\tilde{x}_{i-1}\uparrow\right),\ i=2,3,\ldots,n\end{cases}\end{cases}, \tag{6}$$

where x_i and $\tilde{x}_i$ denote the TI and corresponding reconstruction in the i th training stage. $\tilde{x}_{i-1}\uparrow$ is the tensor obtained through upsampling the outputs in the $(i-1)$ th training stage. $\mathcal{L}_{\mathrm{gp}}$ is the gradient penalty regularization term, with weight coefficient α_{gp} and gradient operator ∇. $\hat{x}$ is a tensor obtained by mixing x_i and $\tilde{x}_i$ with random proportions. P_{g} and P_{r} denote the statistical distributions of both generated and real samples. $\mathbb{E}$ is the mathematical expectation. Based on $\mathcal{L}_{\mathrm{gp}}$, the gradient of loss function fits with 1-Lipschitz constraint so that different training processes in MSGAN are further stabilized. $\mathcal{L}_{\mathrm{rec}}(G_i)$ focuses on the global structural similarity comparison between x_i and $\tilde{x}_i$ following:

$$\mathcal{L}_{\mathrm{rec}}(G_i)=\|\tilde{x}_i-x_i\|_2^2. \tag{7}$$

Therefore, both G and D in different training stages can be optimized through stochastic gradient descent and back propagation, and simulation performance can be improved based on concurrent training pattern and parameter inheritance. Finally, abundant prior samples with diverse geological patterns are generated and used for training BicycleGAN to achieve reservoir conditional simulation.

2.2. Reservoir conditional simulation based on BicycleGAN

BicycleGAN is a kind of end-to-end conditional deep generative framework, which defines the mapping correlation between the input conditioning data and output modes to consider the geological constraints effectively during simulation. It shows a better simulation performance in terms of generation diversity and fine characterization of property information compared with Pix2Pix. Below we detail the theory, network structure, and loss function of BicycleGAN.

2.2.1. Theory and network structure of BicycleGAN

Fig. 3 illustrates the network structure and training process of BicycleGAN, including two different sub-modules named conditional Variational Autoencoder GAN (cVAE-GAN) and conditional Latent Regressor GAN (cLR-GAN). The goal of cVAE-GAN is to finely characterize the heterogeneous reservoir patterns under geological constraints. Specifically, B is firstly input to the encoding function E to get a latent distribution $Q(z|B)$. E herein aims to predict a Gaussian distribution. Then, a latent vector is randomly sampled from $Q(z|B)$, which is integrated with conditioning data A and input into G so that the desired output can be “noisy peeked” to create simulation $\widehat{B}$ (denoted as $B\rightarrow z\rightarrow\widehat{B}$). cLR-GAN embeds the latent feature into the generation process, and the statistical distribution consistency between latent distribution $\mathcal{N}(z)$ and actual test distribution $P(z)$ is gradually recovered. Specifically, a latent code is randomly sampled from Gaussian distribution and input into G along with A. Then, the output is encoded into a latent vector with noisy distribution (marked as $\widehat{z}$) to provide a point estimation (denoted as $z\rightarrow\widehat{B}\rightarrow\widehat{z}$). Meanwhile, two independent D s are used to perform discrimination tasks in cVAE-GAN and cLR-GAN, and corresponding network parameters are optimized through different loss indicators (i.e., adversarial loss, conditional loss, KL loss, latent distribution loss and reconstruction loss).

A bijective consistency between latent code and output mode is defined $(z\leftrightarrow G(A,\ z))$, in which $G(A,z)$ is expected to preserve enough latent information so that E can approximately recover the original latent representation from the generated samples. Rather than the mathematical bijection, the bijective consistency refers to a reversible latent-output correspondence that encourages different vectors to generate various and realistic output modes while preserving latent-space consistency, which can be observed through simulation diversity or quantitatively evaluated by the convergence behavior of latent distribution loss. Therefore, cVAE-GAN ensures the latent codes to capture diverse geological patterns from the training data, while cLR-GAN tries to recover the latent distribution from generation. This dual-path correlation can prevent different latent vectors from generating the same outputs (many-to-one mapping), and the latent space encodes the uncertainty and ambiguity associated with geological patterns effectively, thereby enabling multimodal generation that fits with geological constraints.

Parameters for both G and E are weight-shared except for D. G is composed of convolutional and deconvolutional layers to perform

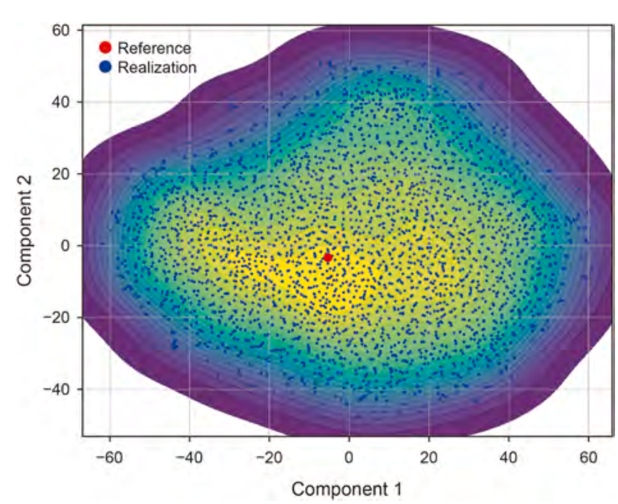

Fig. 6. Feature space distribution for batch simulation of aquifer structural model based on PCA, t-SNE and KDE.

downsampling and upsampling respectively. The main differences are: (1) An Instance Normalization layer was followed by each convolutional and deconvolutional layer instead of Batch Normalization, which normalizes all the channel features of mini-batch samples to reduce the GPU computing overburden; (2) The soft-hard conditioning data and z are used as the input of G. z is firstly expanded to the same size as the soft-hard conditioning data, and then the value of soft-hard conditioning data is normalized into $[-1, 1]$, matching the activation function Tanh at the final output layer. These data are concatenated to form a

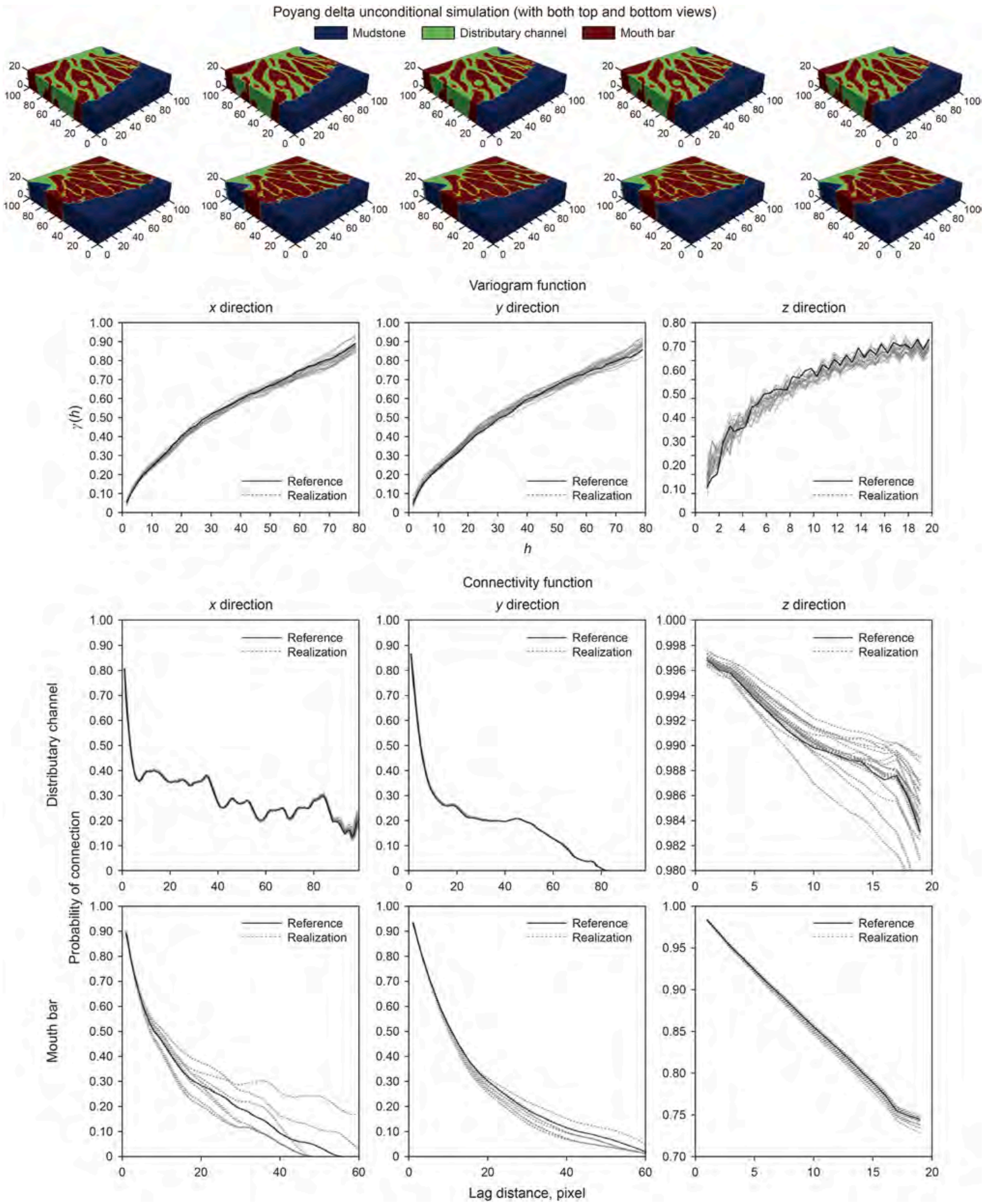

Fig. 7. Unconditional simulation of sedimentary delta model based on MSGAN and quantitative evaluations during batch simulation.

multi-channel hybrid tensor so that G needs to define a transition way from multiple conditioning data to output geological patterns. Among them, the hard conditioning data refers to the real geological observation with a high spatial resolution (i.e., borehole data and geological sections). The soft conditioning data presents the variable distribution uncertainty in terms of probability (i.e., geophysical interpretation and seismic inversion). Therefore, the nonlinear mapping correlation between multiple conditioning data and output modes was defined to improve the reservoir characterization accuracy. The PatchGAN-based Ds were introduced in cVAE-GAN and cLR-GAN, including two sub-frameworks (D_1 and D_2) to perform multiscale discrimination. D_1 is mainly composed of a convolutional layer, while an additional average pooling layer is included in D_2, which outputs two scalar fields under different scales by downsampling input data. Each probability of the scalar fields denotes the discrimination result within the local region, and detailed geological information is better considered during simulation by calculating the average value of scalar matrices. E is mainly composed of residual blocks, which include a main pipeline and a shortcut-connection. By inputting feature maps into the residual block, the outputs of two branches are integrated through element-wise addition so that the size of the final output is half-reduced compared with the input. After one convolutional layer, three residual blocks and one average pooling layer, the dimension of the output latent vector keeps the same as z.

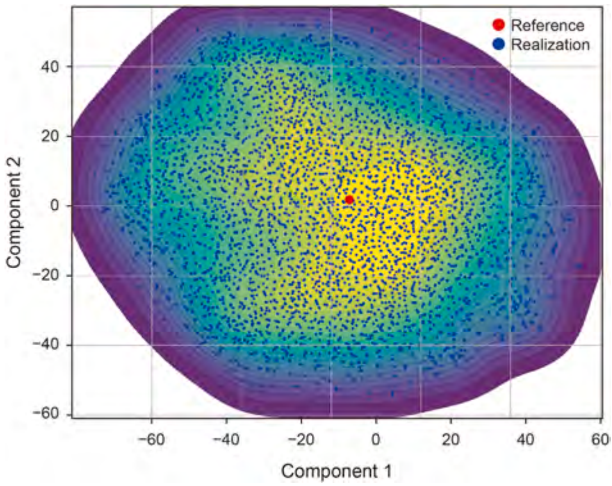

Fig. 8. Feature space distribution for batch simulation of sedimentary delta model based on PCA, t-SNE and KDE.

2.2.2. Loss function of BicycleGAN

A joint loss function, including adversarial loss and conditional loss, is defined to optimize BicycleGAN. Adversarial loss can make BicycleGAN generate geological patterns that are similar to the training samples, while conditional loss can improve the facies

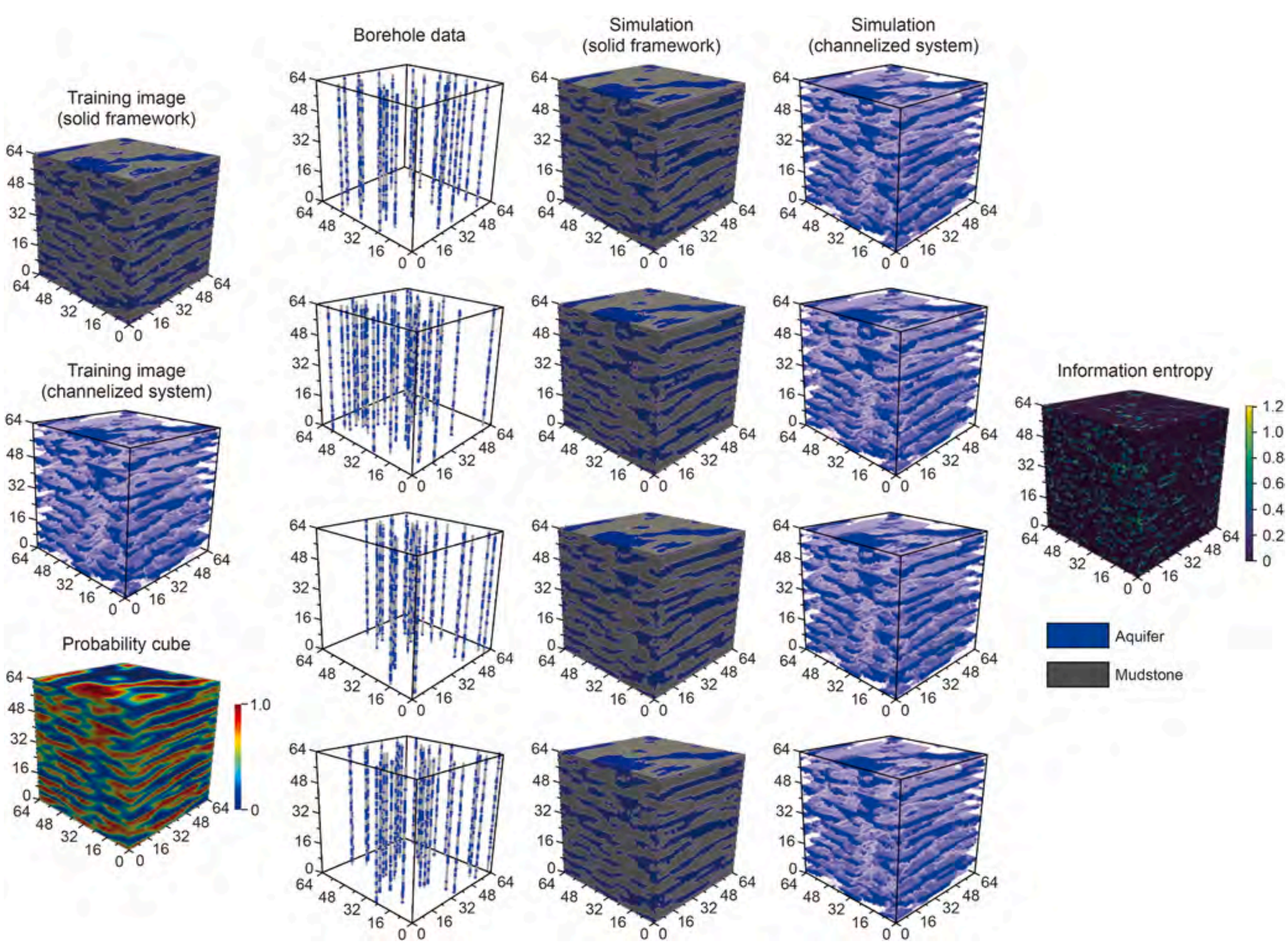

Fig. 9. Conditional simulations of aquifer structural model and uncertainty analysis.

reconstruction accuracy at the location of conditioning data. Therefore, the joint loss function is defined as:

$$\mathcal{L}_{\mathrm{BicycleGAN}}(G,D,E)=\mathcal{L}_{\mathrm{cVAE-GAN}}+\mathcal{L}_{\mathrm{cLR-GAN}}+\lambda_{\mathrm{con}}\cdot\mathcal{L}_{\mathrm{con}}, \tag{8}$$

where $\mathcal{L}_{\mathrm{cVAE-GAN}}$ and $\mathcal{L}_{\mathrm{cLR-GAN}}$ denote the loss function of cVAE-GAN and cLR-GAN, respectively; $\mathcal{L}_{\mathrm{con}}$ is the conditional loss that are only used for hard conditioning data. $\mathcal{L}_{\mathrm{cVAE-GAN}}$ is formulated as:

$$\mathcal{L}_{\mathrm{cVAE-GAN}}(G,D,E)=\mathcal{L}_{\mathrm{GAN}}^{\mathrm{VAE}}(G,D)+\lambda_{L_1}\mathcal{L}_1^{\mathrm{VAE}}(G,E)+\lambda_{\mathrm{KL}}\mathcal{L}_{\mathrm{KL}}(E), \tag{9}$$

where $\mathcal{L}_{\mathrm{GAN}}^{\mathrm{VAE}}$ denotes the prior loss of cVAE-GAN, $\mathcal{L}_1^{\mathrm{VAE}}$ and $\mathcal{L}_{\mathrm{KL}}$ denote the L_1 loss and KL loss respectively. As pixel-level operator, L_1 loss herein focuses on the reconstruction of low-frequency information (i.e., global reservoir structures), while KL loss can evaluate the distribution similarity between $Q(z|B)$ and $\mathcal{N}(z)$. Therefore, $\mathcal{L}_{\mathrm{GAN}}^{\mathrm{VAE}}$ is defined as:

$$\begin{aligned}\mathcal{L}_{\mathrm{GAN}}^{\mathrm{VAE}}(G,D)=&\ \mathbb{E}_{A,B\sim p(A,B)}[\log D(B)]\\&+\mathbb{E}_{A,B\sim p(A,B)}[\log(1-D(G(A,z)))],\end{aligned} \tag{10}$$

where $p(*)$ is the sample distribution, $G(*)$ and $D(*)$ are the outputs of G and D respectively, and $\mathbb{E}$ is the mathematical expectation. $\mathcal{L}_1^{\mathrm{VAE}}(G,E)$ and $\mathcal{L}_{\mathrm{KL}}(E)$ are formulated as:

$$\mathcal{L}_1^{\mathrm{VAE}}(G,E)=\mathbb{E}_{A,B\sim p(A,B),\ddagger\sim E(B)}\|B-G(A,z)\|_1, \tag{11}$$

$$\mathcal{L}_{\mathrm{KL}}(E)=\mathbb{E}_{B\sim p(B)}[\mathcal{D}_{\mathrm{KL}}(E(B)\|\mathcal{N}(0,I))], \tag{12}$$

$$\mathcal{D}_{\mathrm{KL}}(p\|q)=\int p(z)\log\frac{p(z)}{q(z)}\mathrm{d}z, \tag{13}$$

where $\mathcal{D}_{\mathrm{KL}}(E(B)\|\mathcal{N}(0,I))$ denotes the KL divergence calculator between latent distributions $E(B)$ and standard Gaussian distribution $\mathcal{N}(0,I)$. $\mathcal{L}_{\mathrm{cLR-GAN}}$ is defined as:

$$\mathcal{L}_{\mathrm{cLR-GAN}}(G,D,E)=\mathcal{L}_{\mathrm{GAN}}^{\mathrm{cLR}}(G,D)+\lambda_{\mathrm{latent}}\mathcal{L}_1^{\mathrm{latent}}(G,E), \tag{14}$$

where $\mathcal{L}_{\mathrm{GAN}}^{\mathrm{cLR}}(G,D)$ is the prior loss of cLR-GAN, which is same as Eq. (10). $\mathcal{L}_1^{\mathrm{latent}}$ is the evaluation of latent distribution loss, with corresponding weight coefficient $\lambda_{\mathrm{latent}}$. Therefore, $\mathcal{L}_1^{\mathrm{latent}}$ is written as:

$$\mathcal{L}_1^{\mathrm{latent}}(G,E)=\mathbb{E}_{A\sim p(A),z\sim p(z)}\|z-E(G(A,z))\|_1. \tag{15}$$

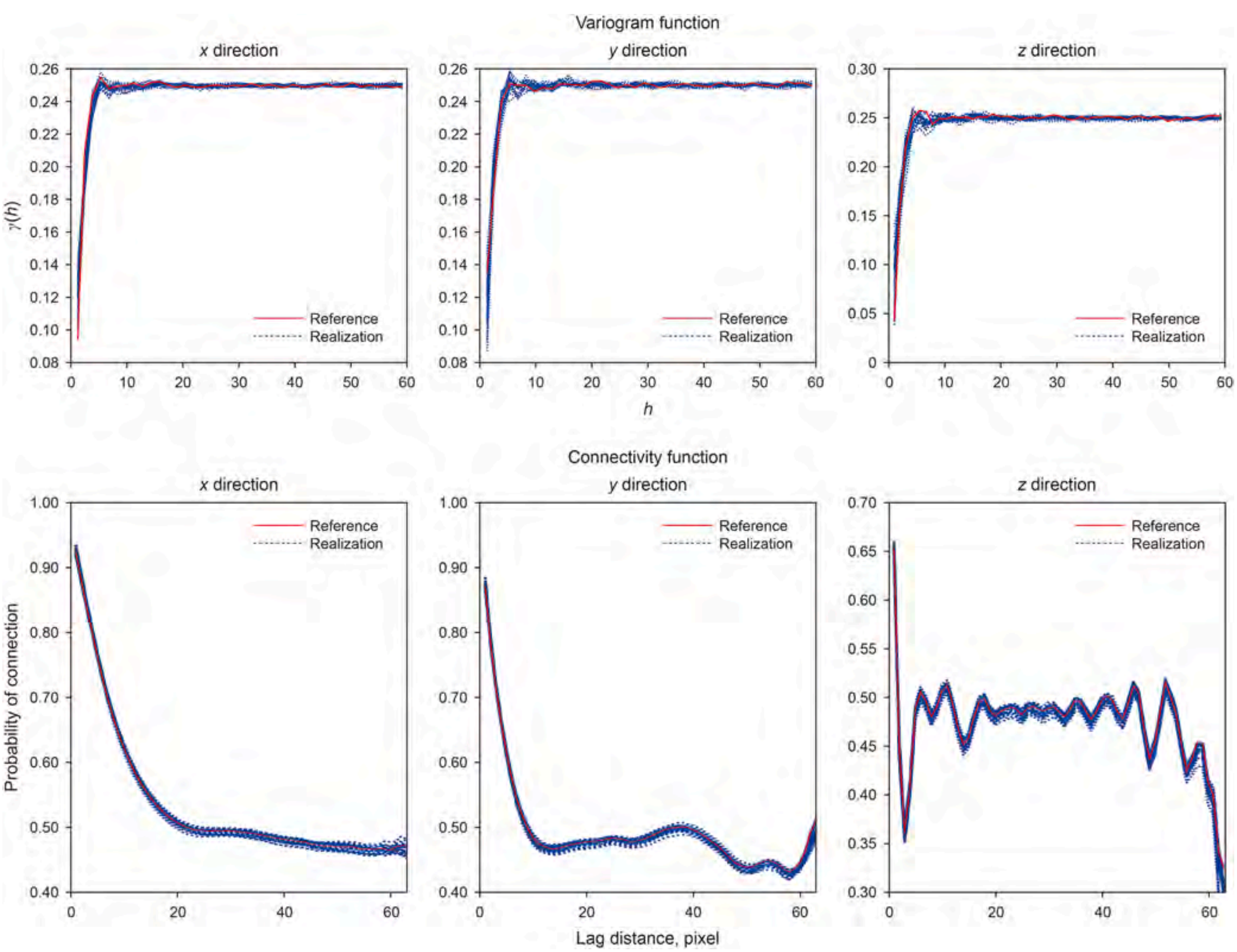

Fig. 10. Variogram model and connectivity function for batch conditional simulation of aquifer structural model.

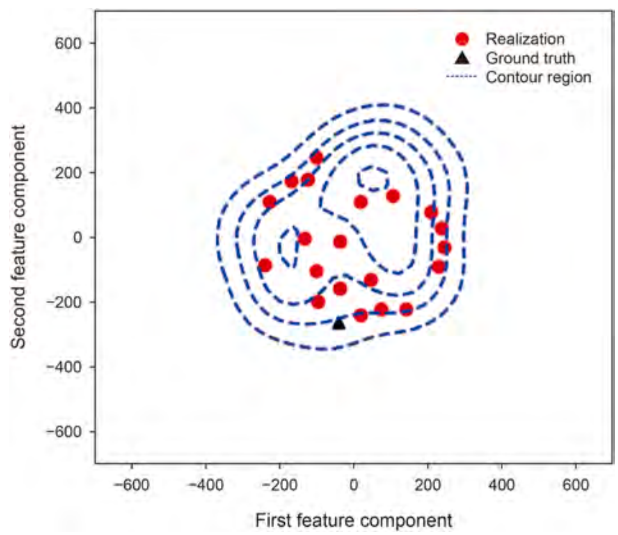

Fig. 11. MDS visualization for batch conditional simulation of aquifer structural model.

Furthermore, $\mathcal{L}_{\text{con}}$ is defined based on L_1 regularization term:

$$\mathcal{L}_{\text{con}} = \|M \odot (G(A,z) - B)\|_1, \tag{16}$$

where M is the binary mask including two elements 0 and 1, denoting the location of non-conditioning and conditioning data. Based on the element-wise product operator $\odot$, facies labels at all well locations are extracted between $G(A,z)$ and B. Though the definition of $\mathcal{L}_{\text{con}}$ and $\mathcal{L}_1^{\text{VAE}}$ are similar to each other, the former one focuses on the facies reconstruction accuracy for single pixel, while the latter one is used for evaluating the global structural discrepancy. Meanwhile, the soft data conditional loss is not considered in the experiment because it is regarded as an auxiliary variable during reservoir simulation. Overall, G, D and E are iteratively optimized based on the joint loss function to achieve conditional reservoir simulation.

3. Synthetic case simulation examples

Two synthetic TIs were used to verify the simulation performance of the proposed approach. Apart from visual

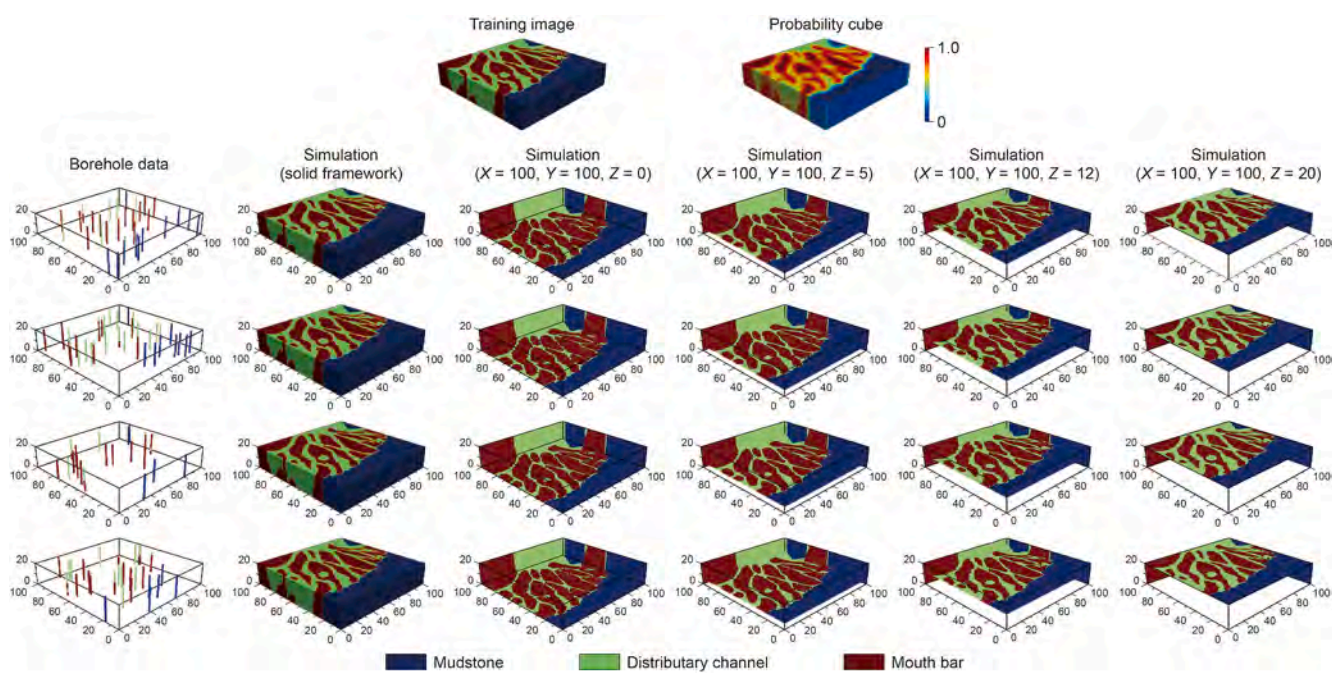

Fig. 12. Conditional simulations of sedimentary delta model, with different layers being presented along vertical directions.

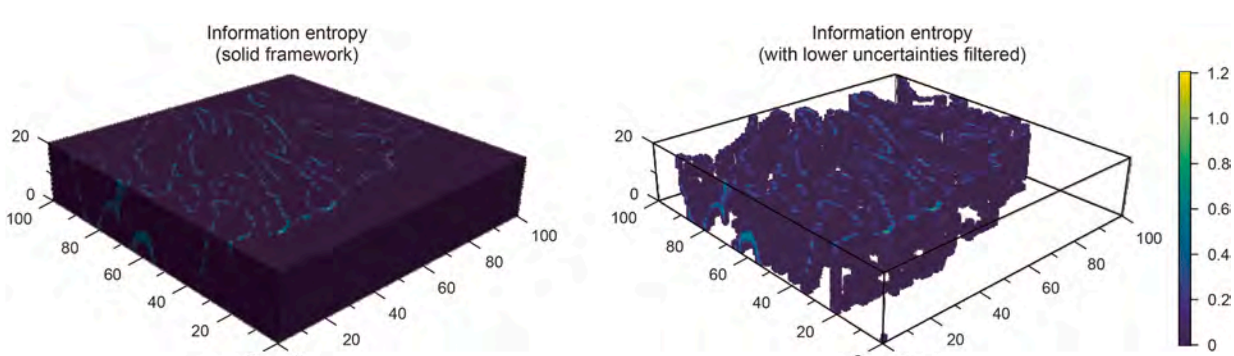

Fig. 13. Uncertainty analysis for batch conditional simulation of sedimentary delta model.

appearance, we used different metrics (i.e., variogram model, connectivity function, and Multi-Dimensional Scaling (MDS)) to evaluate the simulation performance of MSGAN and BicycleGAN. Through parameter sensitivity analysis, we discussed how the parameter variations impact the output modes during data augmentation, and the simulation performance was further compared with that of the traditional approaches. Python 3.9.7 and PyTorch 1.10.1 were selected as the basic compilation framework, and neural networks were trained on a workstation with an Intel Xeon Gold 5117 CPU, 64 GB RAM and a NVIDIA GeForce RTX 4090 TI GPU.

Fig. 4 illustrates two synthetic reservoir TIs (https://github.com/GAIA-UNIL/trainingimages), including an aquifer structural model (size: 64×64×64, unit: voxel) and a sedimentary delta model (size: 100×100×20, unit: voxel), which present significant heterogeneity and anisotropy in the modeling domain. Meanwhile, Table 1 summarizes some parameter settings during training MSGAN and BicycleGAN, which were defined after trial-and-error

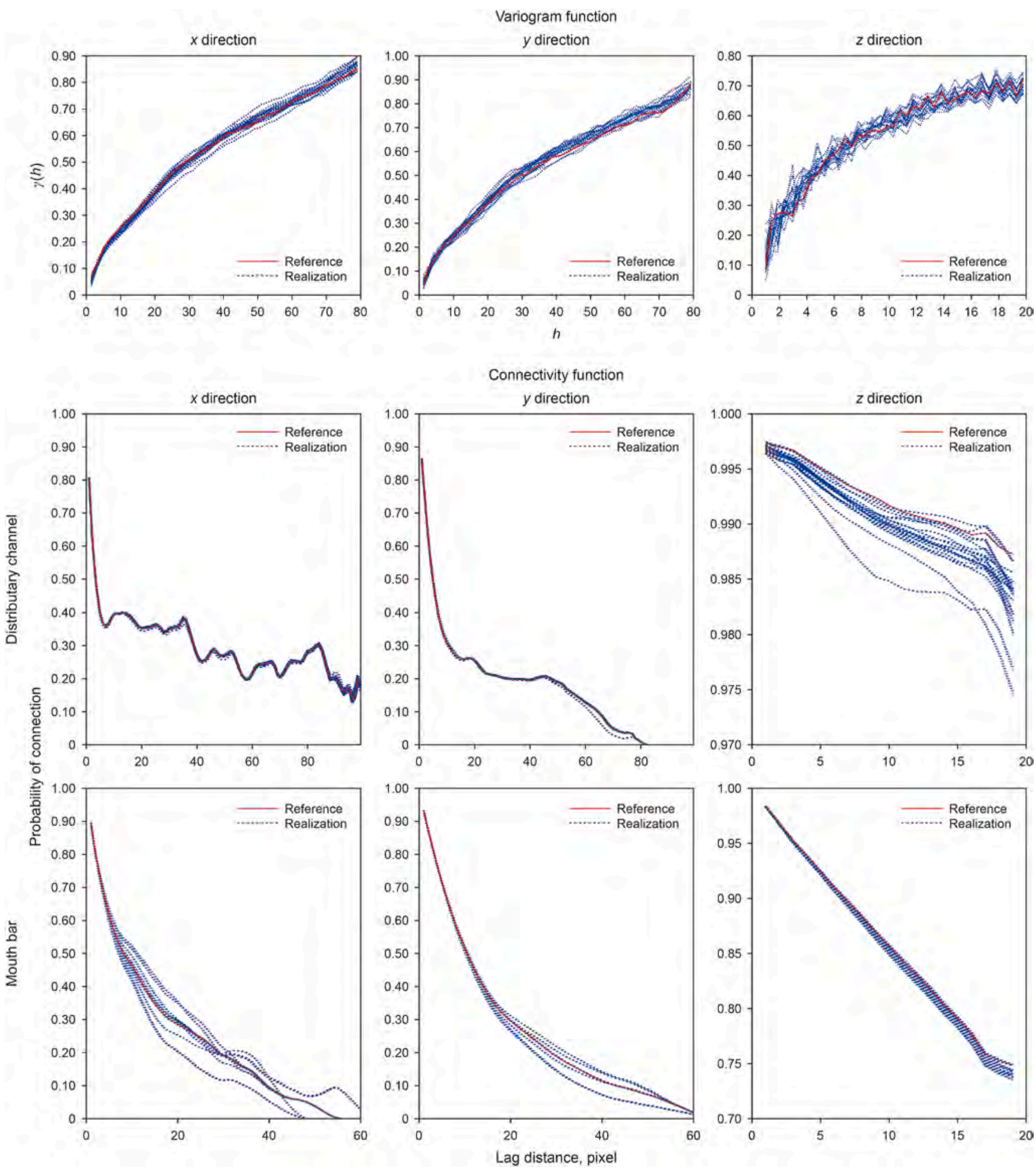

Fig. 14. Variogram model and connectivity function for batch conditional simulation of sedimentary delta model.

based on a small proportion of training datasets. Specific network structures of MSGAN and BicycleGAN for two synthetic cases were summarized in the Supplementary data.

4. Results

Table 2 summarizes the training time consumption and GPU memory usages of MSGAN and BicycleGAN based on two synthetic TIs. Below we detail the simulation performances during data augmentation and conditional simulation under different scenarios.

4.1. Data augmentation based on MSGAN

4.1.1. Aquifer structural model

Some reconstructed geological prior model based on MSGAN are presented in Fig. 5. The heterogeneities of aquifer channels are well reproduced in the modeling domain, with clear geometric boundaries and continuous distributions. It indicates that MSGAN can create multiple realistic and diverse prior aquifer structures. From variogram models, the simulated spatial variabilities along different directions are similar to TI, and corresponding function curves are closely distributed around the reference line. There is a small discrepancy in facies connection probability between batch simulation results and TI, presenting different fluctuations and trends along different directions. The pretrained MSGAN was used to perform 5000 times unconditional simulations, which were firstly reduced in dimension based on PCA, then the differences were visualized in the feature space based on t-SNE and Kernel Density Estimation (KDE) (Fig. 6). These prior samples are uniformly distributed around the central point (TI), while those samples that are far away from the central point present a sparse distribution, with a smooth kernel density profile overall. Therefore, it shows a simulation diversity during data augmentation, maintaining a close spatial correlation compared to TI and providing an abundant prior dataset for training BicycleGAN.

4.1.2. Sedimentary delta model

The nonstationary patterns for different facies are well reproduced during unconditional simulation of sedimentary delta model, without any independently distributed geological units in the modeling domain (Fig. 7). Both mouth bar and distributary channel are continuously distributed, with a high structural similarity compared against TI. The differences are mainly concentrated on the facies boundaries among different simulations. From variogram model (Fig. 7), spatial variabilities along different directions are significantly increased, with corresponding function curves being closely distributed around the reference line. From connectivity function analyses of mouth bar and distributary channel (Fig. 7), the connection probabilities are similar to reference values, with decreasing trends along different directions. 4000 times unconditional simulations were created based on pretrained MSGAN, and after PCA-based dimensionality reduction, t-SNE and KDE, these prior samples are closely distributed around the TI in the feature space, with fewer outliers and a continuous kernel density profile (Fig. 8). Therefore, MSGAN shows a better simulation performance for the data augmentation of sedimentary delta model, creating diverse prior samples to support training BicycleGAN.

4.2. Conditional simulation based on BicycleGAN

The conditioning dataset was predefined for each prior sample. Borehole data with different numbers and distributions were selected as the hard conditioning data. For the soft conditioning data, each prior model was smoothed by a Gaussian kernel with different size to create the probability cube, which is regarded as the geophysical interpretation. These probability cubes have different spatial resolutions, with standard deviation being equal to the pixel size of the Gaussian kernel. Therefore, these predefined datasets were used for training BicycleGAN to achieve the conditional reservoir simulation.

4.2.1. Aquifer structural model

Fig. 9 illustrates the reconstructions based on different borehole data. All the simulated aquifer structural models fit the borehole constraints (facies reconstruction accuracy at all well locations is 100%), and the aquifer channel is continuously developed in the 3D space. Some metrics (i.e., Root Mean Square Error (RMSE), Peak Signal-to-Noise Ratio (PSNR), Structural Similarity Index Measurement (SSIM) and Lorenz coefficient) are used to quantitatively evaluate the aquifer structural model simulation performance. The values for RMSE, PSNR and SSIM for the reconstructed model are 0.258, 11.768 and 0.867 respectively compared against TI, indicating a better reconstruction ability. The Lorenz coefficient is 0.513, which means that the heterogeneous patterns of aquifer channel are reproduced effectively. Meanwhile, we calculated the information entropy (IE) based on batch simulation following:

$$\mathrm{IE}_v = -\sum_{f \in L}\left[TP_v^{(f)} \log TP_v^{(f)}\right], \tag{17}$$

where f is the facies label, L is the total facies label set, T is the simulation times and $P_v^{(f)}$ is the preference probability of f for voxel v. If the IE_v is large, more facies labels might be randomly assigned to v during simulation, with a high uncertainty. The high uncertainties are concentrated on the facies boundaries, indicating a diverse channel geometric shape, while the inner parts for two facies labels have low uncertainties (Fig. 9). From variogram model and connectivity function, the simulated spatial variabilities and channel connectivity probabilities are close to the reference values (Fig. 10). For the MDS visualization, small Euclidean distances are presented in 2D feature space between the simulation and TI, with a uniform distribution in the contour region (Fig. 11). Therefore, based on the geological constraints, the heterogeneous structural properties are well reproduced by BicycleGAN, and all the

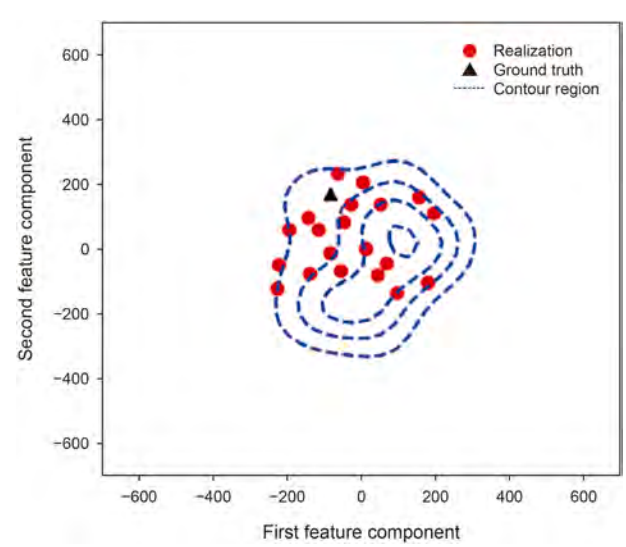

Fig. 15. MDS visualization for batch conditional simulation of sedimentary delta model.

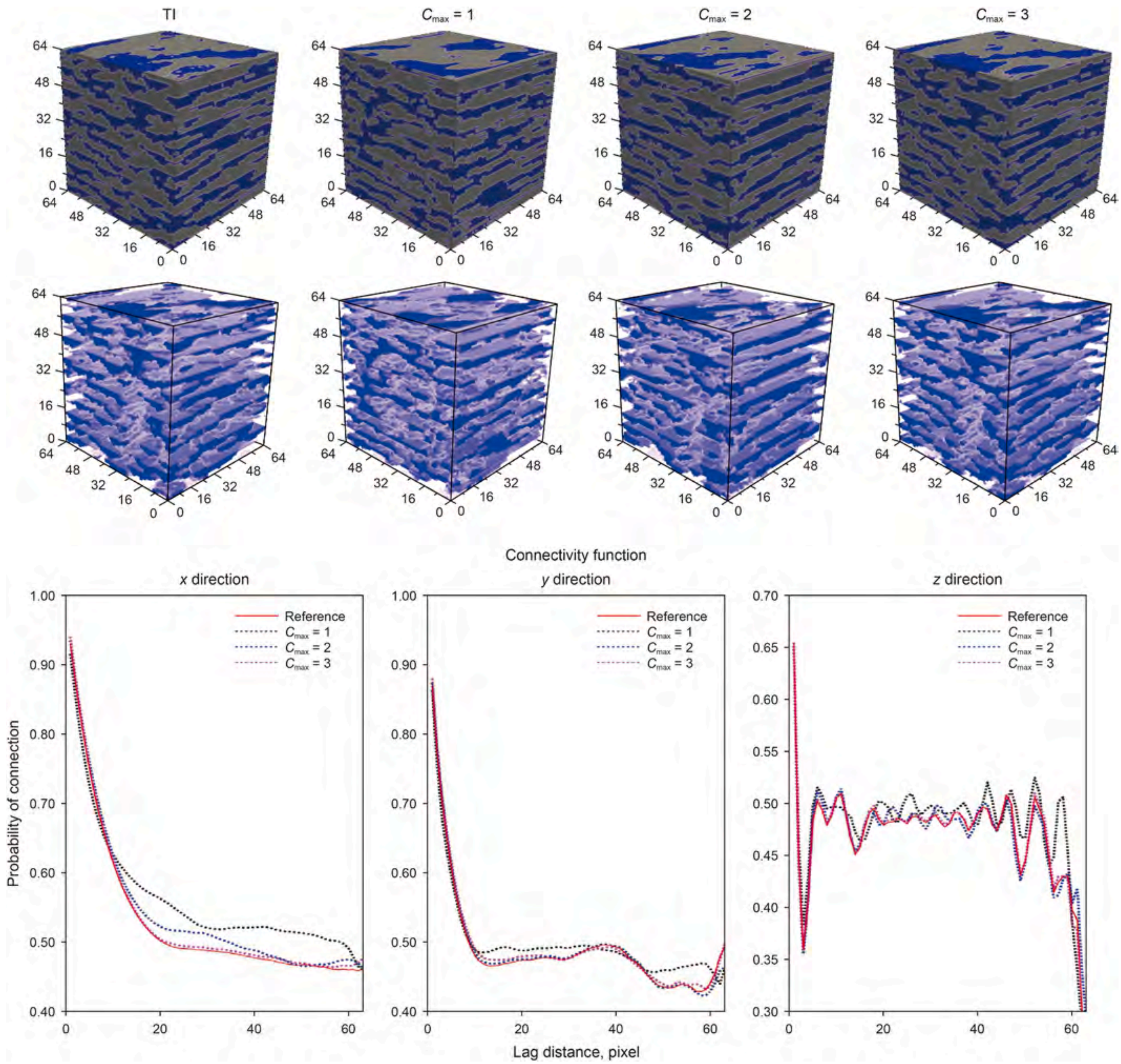

Fig. 16. Parameter sensitivity analysis for unconditional simulation of aquifer structural model based on MSGAN.

simulations are similar to TI in terms of spatial variability, channel connectivity and spatial structures.

4.2.2. Sedimentary delta model

Fig. 12 illustrates four groups of conditional simulation of a sedimentary delta model based on different borehole fields, with different layers being presented along vertical direction. Nonstationary patterns are well constructed by BicycleGAN, without any facies mismatch at well locations. In different layers, geometric shapes of mouth bar and distributary channel are similar to TI, with a continuous and wide distribution in 3D space. From uncertainty analysis, the higher uncertainties are mainly distributed in the facies boundaries, while the inner parts have relatively low uncertainties (Fig. 13). Compared against the TI, the RMSE, PSNR, SSIM and Lorenz coefficient of reconstructed delta are 0.052, 25.743, 0.992 and 0.616 respectively, indicating that the complex nonstationary patterns are effectively reproduced in the modeling domain. From the variogram models (Fig. 14), the simulated spatial variabilities within different h are close to the reference value, presenting upward trends along different directions overall. For mouth bar and distributary channel, the differences of connection probabilities between batch simulation and TI are relatively small

Table 3
Statistical results of Sim_{OD} with different C_{max}, in which the bold Sim_{OD} refer to the optimum C_{max} value for two scenarios.

Values	Sim_{OD}, %	
	Aquifer structural model	Sedimentary delta model
$C_{max} = 1$	56.84	68.35
$C_{max} = 2$	**83.51**	85.06
$C_{max} = 3$	95.07	**88.87**

(Fig. 14). During MDS analysis, the simulated models are uniformly distributed around the TI in the feature space, maintaining significant structural correlations (Fig. 15). Therefore, nonstationary patterns fitting with geological constraints can be constructed based on BicycleGAN, with similar spatial variability and channel connectivity compared against TI.

5. Discussions

5.1. Parameter sensitivity analysis for MSGAN

During training BicycleGAN, some parameters (i.e. z_{dim}) are less sensitive for the conditional simulation performance, and the

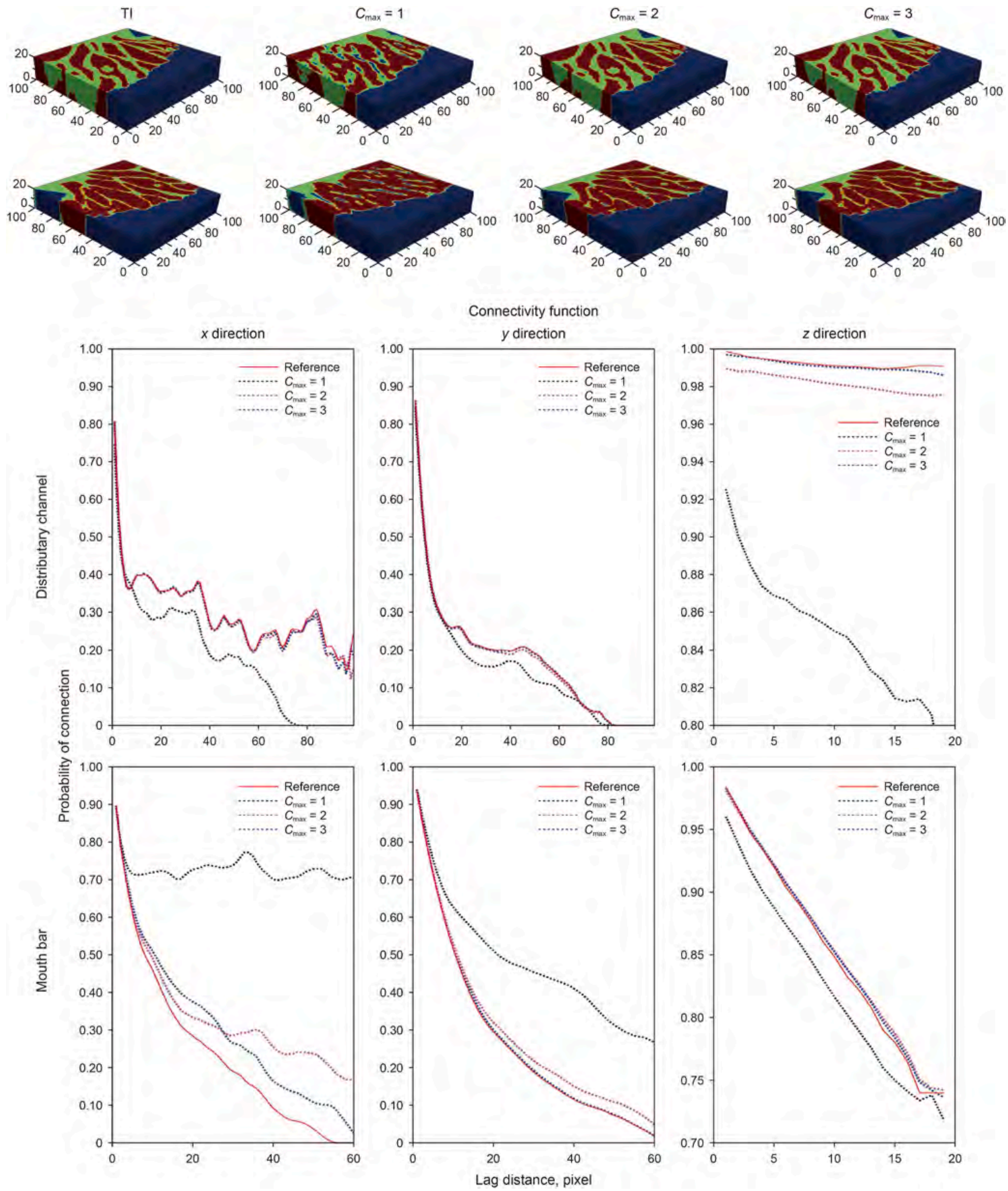

Fig. 17. Parameter sensitivity analysis for unconditional simulation of sedimentary delta model based on MSGAN.

remained ones (i.e., θ_{MSGAN}, λ_{KL} and λ_{L_1}) are set within reasonable ranges through repeatedly fine-tuning. Therefore, the parameter sensitivity analysis of BicycleGAN is not discussed in the paper. For MSGAN, however, two important parameters min_size and num_{train} are closely related to the data augmentation quality (Fan et al., 2024b). Specifically, min_size reflects the minimum size of the generated image at the initial training stage, with global structures being extracted by the receptive fields. If min_size is too large, the global information cannot be well characterized, thereby impacting the simulation performance at subsequent training

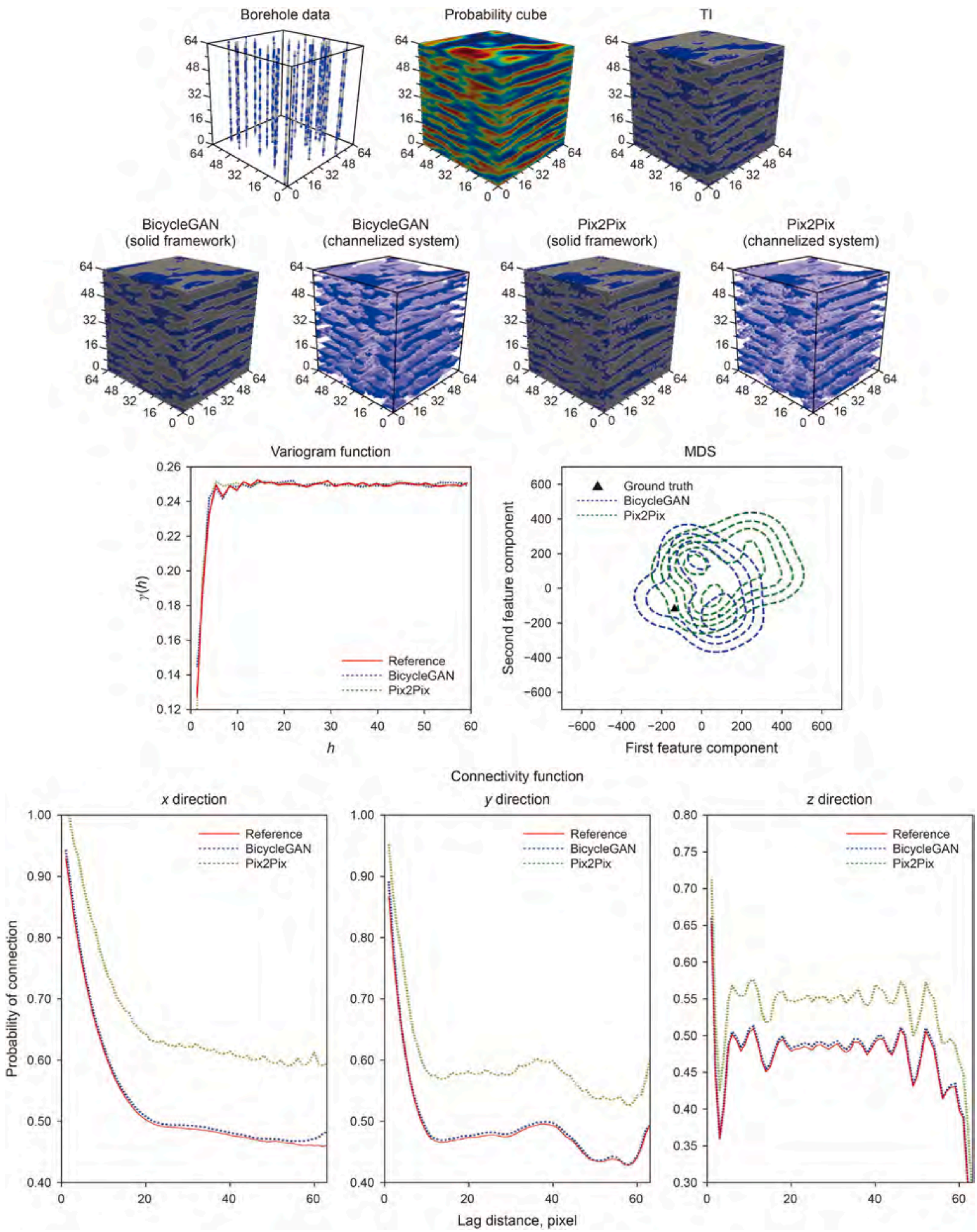

Fig. 18. Comparative results for aquifer structural model reconstruction between BicycleGAN and Pix2Pix.

stages. Furthermore, num_{train} directly controls the number of training stages in MSGAN. If num_{train} is too low, the heterogeneous geological patterns cannot be well reproduced, with some independent channel bodies being randomly distributed in the modeling domain. With num_{train} increasing, though complex geological patterns can be reproduced effectively, a huge computing overburden might exist. Referring to Fan et al. (2024b), both min_size and num_{train} are set as 10×10×10 and 5 respectively for two synthetic cases so that the relationship between simulation performance and computing efficiency is well balanced.

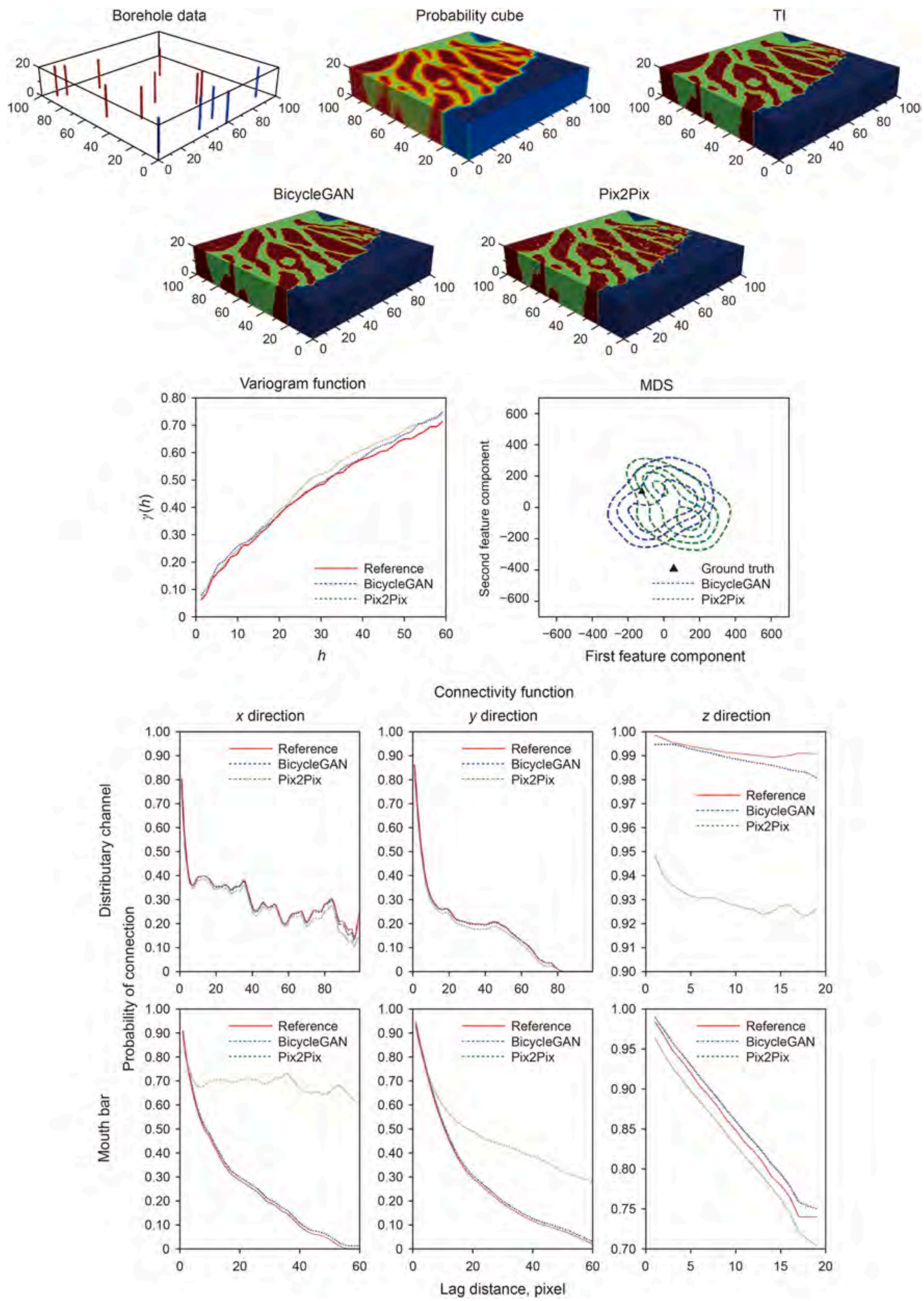

Fig. 19. Comparative results for sedimentary delta model reconstruction between BicycleGAN and Pix2Pix.

Furthermore, we also found that the range of C_{max} also impacts the simulation performance of MSGAN because it controls the number of Gs in the training sequence. Specifically, when C_{max} is set as 1, only one G is trained in the current training stage, which might impact the network convergence speed and geological pattern extraction. The number of Gs in the training sequence increases gradually by enlarging C_{max}, which can not only cause additional GPU computing overburden, but also impact the generation diversity. Therefore, by fixing other hyperparameters, we discussed how C_{max} impacts the MSGAN simulation performance in this section. An estimator named overfitting degree ($\mathrm{Sim_{OD}}$) was defined to compare the similarity degree between the simulation and TI:

$$\mathrm{Sim_{OD}} = \frac{\sum_{i=1}^{S} I\left(V_i^{\mathrm{sim}} = V_i^{\mathrm{TI}}\right)}{S}, \tag{18}$$

where S is the total number of simulation grids, V_i is the voxel index and $I(*)$ is an indicator function. If the facies label between V_i^{sim} and V_i^{TI} is the same, then $I(*)$ equals to 1, otherwise, $I(*)$ equals to 0. Therefore, if the percentage of $\mathrm{Sim_{OD}}$ is too large, it indicates a poor generation diversity during data augmentation. In contrast, if $\mathrm{Sim_{OD}}$ is too small, though the differences between simulation and TI are significant, heterogeneous geological patterns might not be well reproduced.

For two synthetic cases, C_{max} was defined as 1, 2 and 3 respectively to verify the simulation performance of MSGAN. For aquifer structural model, there is a poor channel continuity when $C_{max} = 1$, with a large discrepancy of connection probabilities compared against the reference value. By increasing C_{max}, however, the simulation performance of MSGAN is gradually improved, especially when $C_{max} = 3$, the simulation is too similar with TI, and the connection probabilities are almost the same as the reference value, with a highest $\mathrm{Sim_{OD}}$ (95.07%) (Fig. 16 and Table 3). Therefore, by setting $C_{max} = 2$, the simulation performance and generative diversity of aquifer structural model are well balanced. For sedimentary delta model, when $C_{max} = 1$, geometric shapes of both mouth bar and distributary channel are not developed continuously, and corresponding connection probabilities are far away from the reference value. Though the simulation performance is improved by setting $C_{max} = 2$, some artifacts still exist in the modeling domain. When $C_{max} = 3$, these artifacts are completely depressed, and connection probabilities for mouth bar and distributary channel are close to the reference value, with the best simulation performance overall ($\mathrm{Sim_{OD}}$ is smaller than 90%) (Fig. 17 and Table 3). Therefore, C_{max} should be set within a reasonable range so that MSGAN can provide realistic and diverse simulations during data augmentation.

5.2. Comparative study with Pix2Pix

The simulation performance between BicycleGAN and Pix2Pix was compared based on two synthetic TIs. Pix2Pix can realize the style transformation between two image domains. For reservoir modeling, the conditioning data can be directly input into Pix2Pix to obtain the reconstructions (Isola et al., 2017). The hard conditioning data were only input into the G in Pix2Pix, and one PatchGAN-based D was used in Pix2Pix to perform discrimination task. During training process, the loss function for Pix2Pix was combined with adversarial loss and L_1 regularization term. We fixed the borehole field distribution during comparative study, and results show that the geometric shape of aquifer channels constructed by Pix2Pix is not clear, with some artifacts existing in the 3D space, while the reconstructions based on BicycleGAN have a better visual appearance (Fig. 18). The spatial variability simulated based on BicycleGAN is closer to the reference value, and the channel connectivity is more continuous than that of Pix2Pix. MDS analysis also indicates that the contour region of batch simulation based on BicycleGAN is close to the TI in the feature space, while for Pix2Pix-based batch simulation, the contour region is deviated from the TI. For sedimentary delta model simulation, though nonstationary patterns are effectively reproduced by both frameworks, there are some noises in the models constructed by Pix2Pix (Fig. 19). We inferred that due to the L_1 regularization, Pix2Pix mainly focuses on the global pattern reconstruction while detailed features are overlooked. Quantitative evaluations indicate that simulation performance of BicycleGAN is more advanced than that of Pix2Pix in terms of spatial variability, channel connectivity and spatial structures. Overall, high-order statistical properties of training samples are well extracted by BicycleGAN so that both global patterns and local detailed features are considered simultaneously, revealing a great potential in the heterogeneous reservoir conditional simulation.

5.3. Comparative study with Conditional Image Quilting (CIQ)

In this section, we compared the simulation performance between BicycleGAN and Conditional Image Quilting (CIQ). CIQ is a kind of pattern-based stochastic simulation approach, which links multiple patches extracted from TI to improve the facies continuity in overlap regions. Meanwhile, both dynamic programming and template splitting are introduced to fit geological constraints (Mahmud et al., 2014). Some main parameter settings and corresponding functions are listed in Table 4. For comparison of aquifer structural model simulation, channel boundaries are clearly characterized by BicycleGAN. The simulated spatial variabilities, channel connectivity and spatial structures based on BicycleGAN are better than those of CIQ (Fig. 20). For the sedimentary delta model simulation, the nonstationary patterns for mouth bar and distributary channel are reproduced by BicycleGAN, while a less continuous geometric shape is presented for the reconstruction of CIQ, with some independently distributed reservoir units existing in 3D space. From quantitative analyses, spatial variabilities, channel connectivity and heterogeneity of sedimentary delta are well characterized by BicycleGAN compared against CIQ (Fig. 21). Overall, BicycleGAN is more suitable for the heterogeneous reservoir simulation than CIQ.

Table 4
Parameter settings for CIQ simulation.

Parameters	Functions	TI categories	
		Aquifer structural model	Sedimentary delta model
S_{overlap}	Control the continuity and diversity between two geological patches	$8 \times 8 \times 8$	$12 \times 12 \times 2$
S_{patch}	Relate to the simulated structural scale	$3 \times 3 \times 3$	$3 \times 3 \times 1$
$\mathrm{num_{replicates}}$	Determine the diversity of candidate patches at different steps	5	5
w_{con}	Balance conditioning accuracy against overlap errors	0.8	0.8

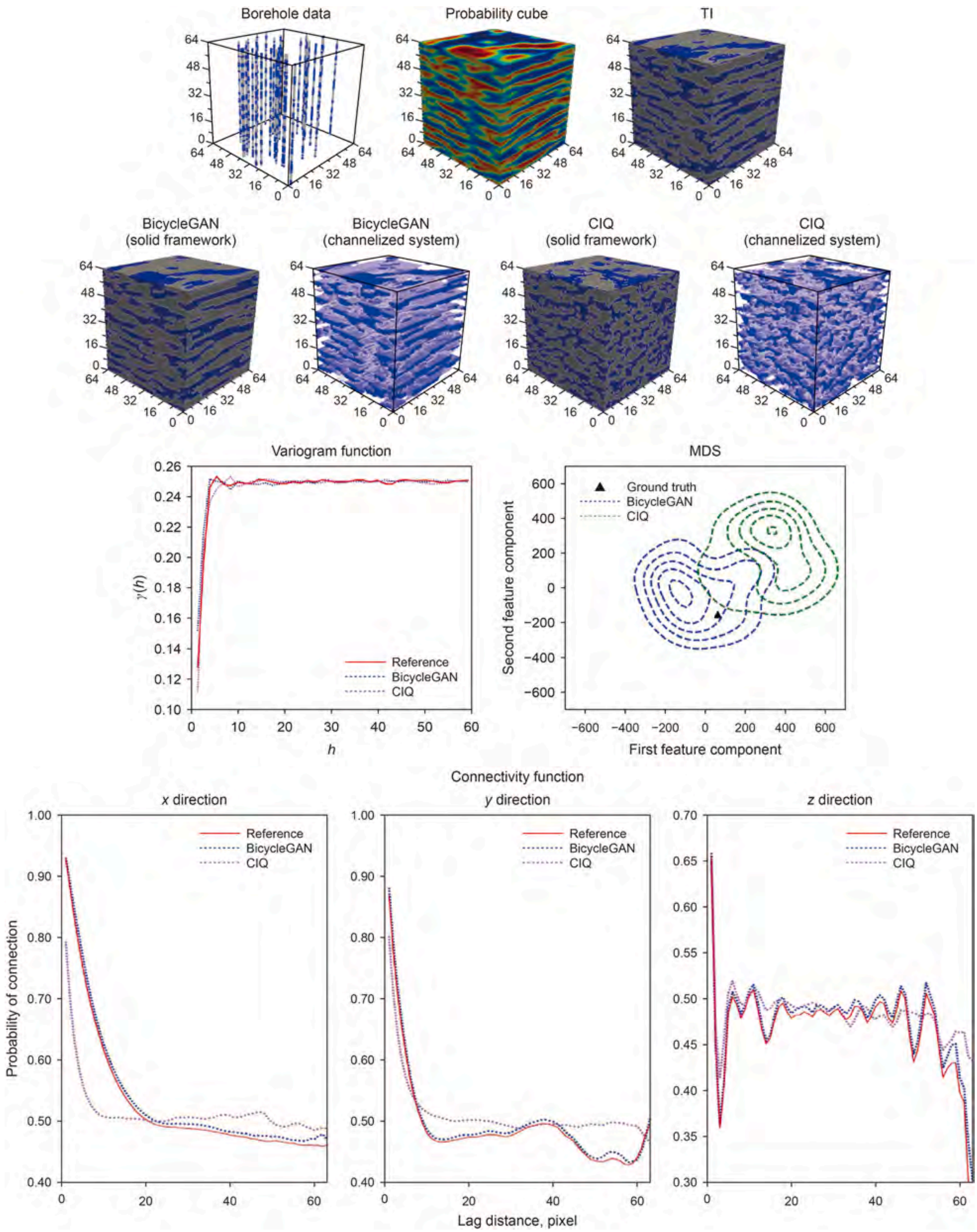

Fig. 20. Comparative results for aquifer structural model reconstruction between BicycleGAN and CIQ.

5.4. Field application

Finally, the proposed modeling framework was introduced into the Norne oil field subsurface modeling. A 2D full-stack seismic section (size: 109×75, unit: pixel) was extracted from a 3D seismic survey (Fig. 22(b)), which extends for 1400 m laterally, and covers a vertical interval of 267 ms two-way time. The region presents a sedimentary trend from shallow marine to fluvio-deltaic, with one exploration well existing in the section profile (Fig. 22(c)) (Miele and Azevedo, 2024). We firstly created the TI referring to existed

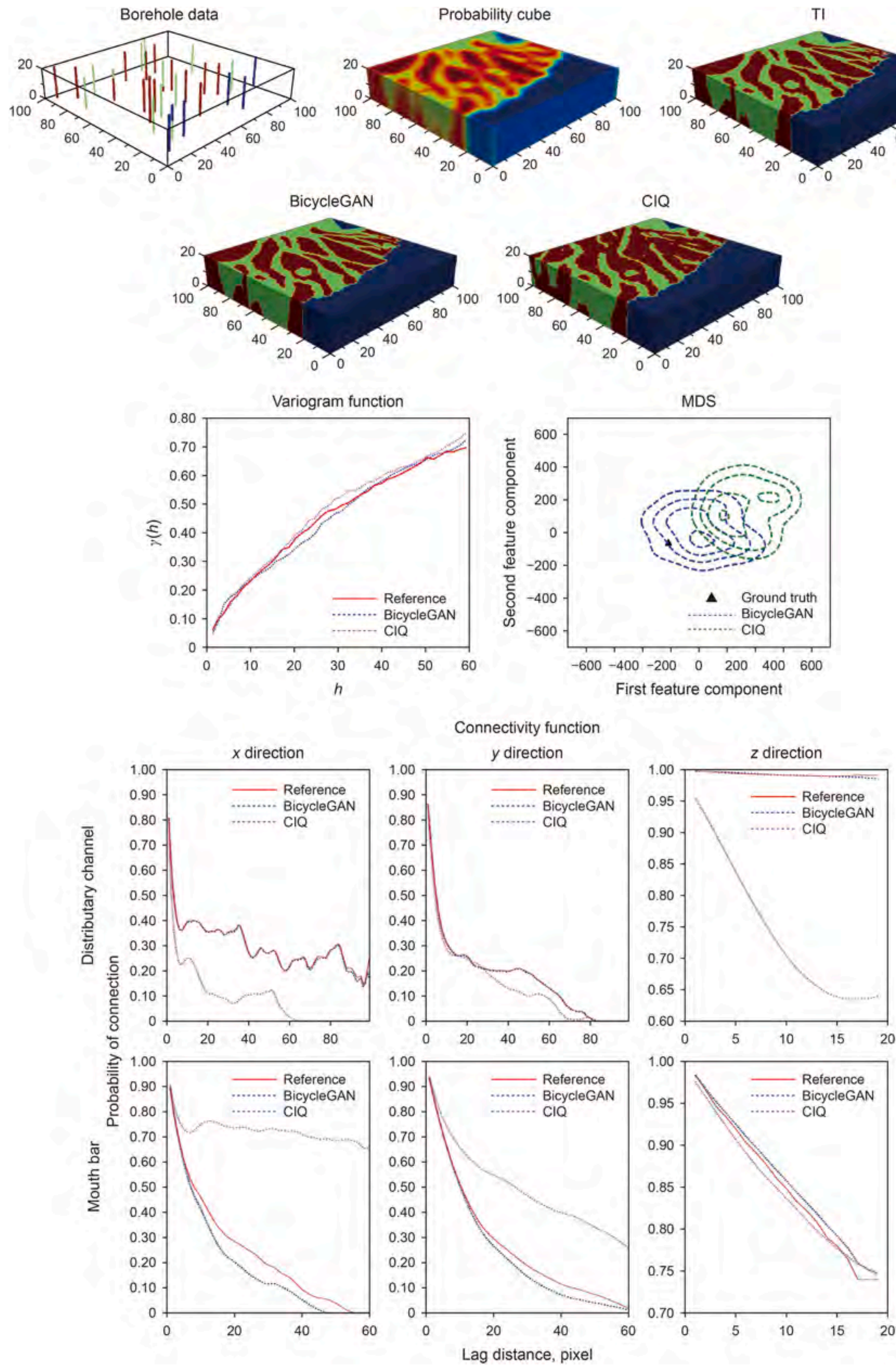

Fig. 21. Comparative results for sedimentary delta model reconstruction between BicycleGAN and CIQ.

geological knowledge, in which mudstone units are randomly developed in the sandstone field (Fig. 22(a)). Then, the pretrained MSGAN was used to generate 4500 unconditional simulations, with some prior patterns being presented in Fig. 22(d). For each prior sample, a different number of boreholes parallel to y-axis were randomly selected as the hard conditioning data. We herein selected the seismic data as the soft conditioning data. Referring to the acoustic impedance value (I_P) distribution at well location, the

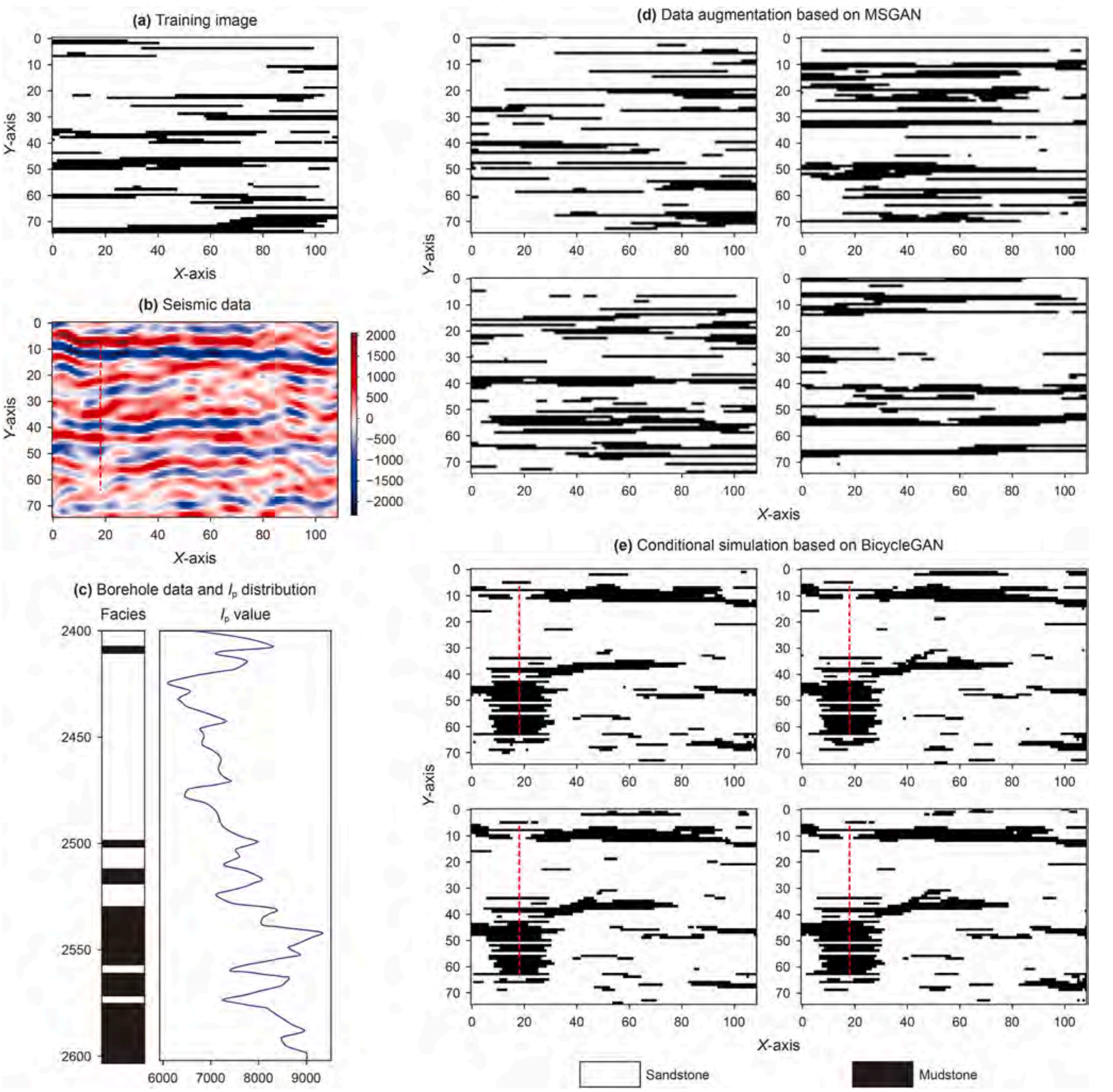

Fig. 22. Modeling results based on MSGAN and BicycleGAN: **(a)** Training Image at Norne oil field; **(b)** full-stack seismic data; **(c)** borehole data and I_P value distribution; **(d)** data augmentation based on MSGAN; **(e)** conditional simulation based on BicycleGAN constrained by (b) and (c).

Direct Sequential Simulation (DSS) (Soares, 2001) was used to create the I_P model for each sample (spherical variogram model, no nugget effect, and the range was set as 10 m), and corresponding synthetic seismic data was created based on a known source wavelet and forward modeling process. Therefore, different training data pairs including borehole data, seismic data and TIs were used for training BicycleGAN. During testing stage, both well data and real seismic data were input into the pretrained BicycleGAN to reproduce the subsurface structures. Specific network parameter settings were provided in the Supplementary data. Different modeling results present significant heterogeneous patterns in the modeling domain, without any facies mismatch at well location (red dashed line in Fig. 22(e)). Furthermore, we calculated the variogram model and connectivity function based on batch conditional simulation (Fig. 23). These simulated spatial variabilities and connection probabilities are close to the reference values, with corresponding function curves keeping a similar trend compared against the reference lines. Since there is only one existing well in the modeling region, and the modeling reliability might be reduced if the synthetic virtual borehole is included, therefore, the 2D application is mainly illustrated in this chapter. However, the proposed modeling framework can also be applied to 3D scenarios. For each 3D prior sample simulated by MSGAN, we can randomly select borehole data in the modeling domain, then create the corresponding I_P model through DSS based on facies acoustic impedance distribution, and synthetic seismic data can be obtained through forward modeling based on the source wavelet. Consequently, the nonlinear mapping between two different

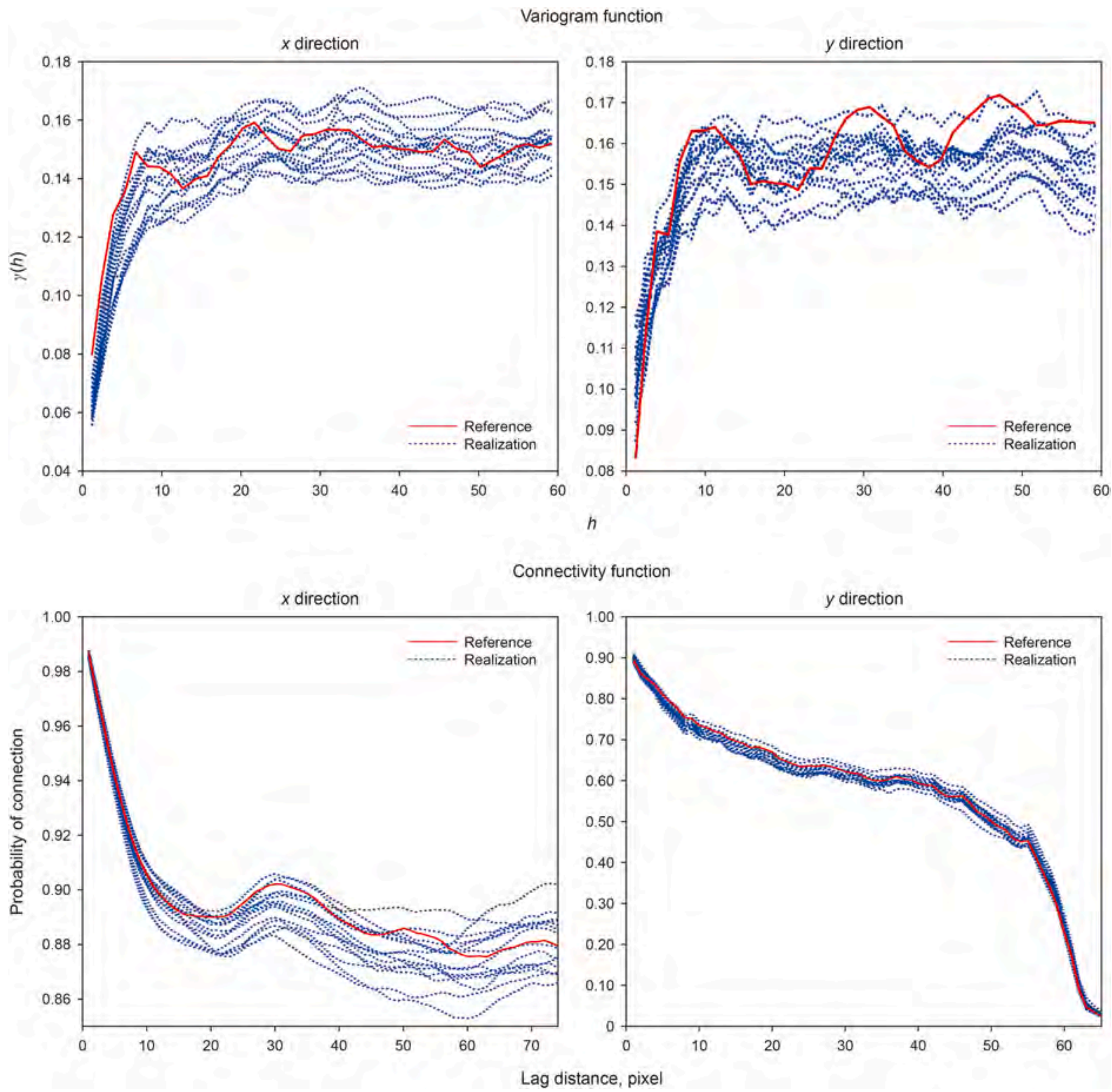

Fig. 23. Variogram model and connectivity functions based on batch conditional simulation.

geological domains (i.e., conditioning dataset and geological patterns) can be learned by BicycleGAN, thereby constructing the real 3D subsurface models based on real borehole field and 3D seismic data.

6. Conclusions

This paper presents a hybrid reservoir modeling framework integrating with MSGAN and BicycleGAN, addressing the challenges in terms of prior geological pattern generation, complex pattern quantification, and conditional simulation with multiple geological constraints. Specifically, based on the multiscale representation of the pyramid structure, MSGAN can extract both global features and local details under small-scale and large-scale respectively. With the multi-stage generation and a series optimization strategy, MSGAN can output diverse and realistic prior geological patterns to support BicycleGAN's training. For BicycleGAN, with the joint effort of cVAE-GAN and cLR-GAN, the bijective consistency between latent codes and output modes is defined to avoid many-to-one-mapping. Through the joint loss function optimization, the multi-modal translation from conditioning dataset to realistic reservoir patterns can be achieved.

However, the proposed framework still has some limitations, such as the weak interpretability during generation and complexity of fine-tuning different parameters. To address these issues, the future outlook will focus on two aspects: (1) enhancing interpretability by traversing latent semantic space to identify optimal latent vectors and visualizing feature propagation across layers, thereby providing theoretical support for uncertainty quantification; and (2) developing an adaptive parameter fine-tuning strategy based on meta-learning and multi-objective optimization instead of manual trial-and-error, ensuring all the parameters are close to the global optimal interval.

CRediT authorship contribution statement

Xue-Chao Wu: Writing – original draft, Investigation, Funding acquisition, Formal analysis, Conceptualization. **Wen-Yao Fan:**

Writing – review & editing, Supervision, Software, Methodology, Investigation. **Shi-Jie Peng:** Supervision, Investigation, Funding acquisition. **Xin-Hua Xu:** Visualization, Investigation. **Feng Deng:** Writing – review & editing, Software. **Xi-Xi Du:** Software, Investigation.

Data availability

The analysis datasets during the current study are available from the corresponding author on reasonable request.

Code availability

The referring codes for synthetic case are given at the link: https://github.com/FANCUG1/Con_MSUGAN, https://github.com/junyanz/BicycleGAN.

Declaration of competing interest

The authors declare that they have no known competing financial interests or personal relationships that could have appeared to influence the work reported in this paper.

Acknowledgements

This work was supported by the 2026 Hubei Provincial Natural Science Foundation Joint Fund Cultivation Project (Grant No. 2026AFC0027), and the Scientific and Technological Research Project of the Hubei Provincial Department of Education (Grant No. B2025130). Meanwhile, we are grateful to the anonymous referees for their insightful comments and suggestions for improving the research enclosed in this paper.

Supplementary data

Supplementary data to this article can be found online at https://doi.org/10.1016/j.petsci.2026.07.009.

References

Abulkhair, S., Madani, N., 2022. Stochastic modeling of iron in coal seams using two-point and multiple-point geostatistics: A case study. Min. Metall. Explor. 39 (3), 1313–1331. https://doi.org/10.1007/s42461-022-00586-0.
Aggarwal, A., Mittal, M., Battineni, G., 2021. Generative adversarial network: An overview of theory and applications. Int. J. Inf. Manag. Data Insights 1 (1), 100004. https://doi.org/10.1016/j.jjimei.2020.100004.
Caers, J., 2011. Modeling Uncertainty in the Earth Sciences. John Wiley & Sons. https://doi.org/10.1002/9781119995920.
Chen, Q., Mariethoz, G., Liu, G., et al., 2018. Locality-based 3-D multiple-point statistics reconstruction using 2-D geological cross sections. Hydrol. Earth Syst. Sci. 22 (12), 6547–6566. https://doi.org/10.5194/hess-22-6547-2018.
Creswell, A., White, T., Dumoulin, V., et al., 2018. Generative adversarial networks: An overview. IEEE Signal Process. Mag. 35 (1), 53–65. https://doi.org/10.1109/MSP.2017.2765202.
Cui, Z., Chen, Q., Liu, G., et al., 2024. SA-RelayGANs: A novel framework for the characterization of complex hydrological structures based on GANs and self-attention mechanism. Water Resour. Res. 60 (1), e2023WR035932. https://doi.org/10.1029/2023WR035932.
Cui, Z., Jiang, S., Chen, Q., et al., 2025. Characterization of reservoir structures with knowledge-informed neural network. SPE J. 30 (8), 4469–4486. https://doi.org/10.2118/228279-PA.
Fan, W., Azevedo, L., Liu, G., et al., 2025. Automatic reconstruction of 3D geological models based on recurrent neural network and predictive learning. Comput. Geosci. 204, 105996. https://doi.org/10.1016/j.cageo.2025.105996.
Fan, W., Liu, G., Chen, Q., et al., 2024a. Automatic reconstruction of geological reservoir models based on conditioning data constraints and BicycleGAN. Geoenergy Sci. Eng. 234, 212690. https://doi.org/10.1016/j.geoen.2024.212690.
Fan, W., Liu, G., Chen, Q., et al., 2024b. Stochastic reconstruction of geological reservoir models based on a concurrent multi-stage U-Net generative adversarial network. Comput. Geosci. 186, 105562. https://doi.org/10.1016/j.cageo.2024.105562.
Goodfellow, I., Bengio, Y., Courville, A., et al., 2016. Deep Learning, vol. 1. MIT Press, Cambridge.
Grana, D., Mukerji, T., Doyen, P., 2021. Seismic Reservoir Modeling: Theory, Examples, and Algorithms. Wiley-Blackwell, Hoboken.
Hosseinzadeh, M., Tavakoli, V., 2024. Analyzing the impact of geological features on reservoir heterogeneity using heterogeneity logs: A case study of Permian reservoirs in the Persian Gulf. Geoenergy Sci. Eng. 237, 212810. https://doi.org/10.1016/j.geoen.2024.212810.
Isola, P., Zhu, J.Y., Zhou, T., et al., 2017. Image-to-image translation with conditional adversarial networks. In: 2017 IEEE Conference on Computer Vision and Pattern Recognition (CVPR). IEEE, pp. 5967–5976. https://doi.org/10.1109/CVPR.2017.632.
Khalili, Y., Ahmadi, M., 2023. Reservoir modeling & simulation: Advancements, challenges, and future perspectives. J. Chem. Pet. Eng. 57 (2), 343–364. https://doi.org/10.22059/jchpe.2023.363392.1447.
Krishnan, S., 2008. The tau model for data redundancy and information combination in Earth sciences: Theory and application. Math. Geosci. 40 (6), 705–727. https://doi.org/10.1007/s11004-008-9165-5.
Levy, S., Friedli, L., Mariéthoz, G., et al., 2024. Conditioning of multiple-point statistics simulations to indirect geophysical data. Comput. Geosci. 187, 105581. https://doi.org/10.1016/j.cageo.2024.105581.
Li, L., Srinivasan, S., Zhou, H., et al., 2015. Two-point or multiple-point statistics? A comparison between the ensemble Kalman filtering and the ensemble pattern matching inverse methods. Adv. Water Resour. 86, 297–310. https://doi.org/10.1016/j.advwatres.2015.05.014.
Li, T., Gong, W., Tang, H., 2021. Three-dimensional stochastic geological modeling for probabilistic stability analysis of a circular tunnel face. Tunn. Undergr. Space Technol. 118, 104190. https://doi.org/10.1016/j.tust.2021.104190.
Liang, Y., Wang, S., Feng, Q., et al., 2024. Ultrahigh-resolution reconstruction of shale digital rocks from FIB-SEM images using deep learning. SPE J. 29 (3), 1434–1450. https://doi.org/10.2118/218397-PA.
Liao, Q., Wang, B., Chen, X., et al., 2024. Reservoir stimulation for unconventional oil and gas resources: Recent advances and future perspectives. Adv. Geo-Energy Res. 13 (1), 7–9. https://doi.org/10.46690/ager.2024.07.02.
Madalimov, M., Li, D., Haynes Jr., B., et al., 2025. Heterogeneity modeling and heterogeneity-based upscaling for reservoir characterization and simulation. SPE J. 30 (2), 942–956. https://doi.org/10.2118/217511-PA.
Mahmud, K., Mariethoz, G., Caers, J., et al., 2014. Simulation of Earth textures by conditional image quilting. Water Resour. Res. 50 (4), 3088–3107. https://doi.org/10.1002/2013WR015069.
Mariethoz, G., Caers, J., 2014. Multiple-Point Geostatistics: Stochastic Modeling with Training Images. John Wiley & Sons. https://doi.org/10.1002/9781118662953.
Miele, R., Azevedo, L., 2024. Physics-informed W-Net GAN for the direct stochastic inversion of fullstack seismic data into facies models. Sci. Rep. 14, 5122. https://doi.org/10.1038/s41598-024-55683-5.
Mishra, A., Sharma, A., Patidar, A.K., 2022. Evaluation and development of a predictive model for geophysical well log data analysis and reservoir characterization: Machine learning applications to lithology prediction. Nat. Resour. Res. 31 (6), 3195–3222. https://doi.org/10.1007/s11053-022-10121-z.
Ronneberger, O., Fischer, P., Brox, T., 2015. U-Net: Convolutional networks for biomedical image segmentation. In: Medical Image Computing and Computer-Assisted Intervention – MICCAI 2015. Springer, Cham, pp. 234–241. https://doi.org/10.1007/978-3-319-24574-4_28.
Sakki, G.K., Tsoukalas, I., Kossieris, P., et al., 2022. Stochastic simulation-optimization framework for the design and assessment of renewable energy systems under uncertainty. Renew. Sustain. Energy Rev. 168, 112886. https://doi.org/10.1016/j.rser.2022.112886.
Salakhutdinov, R., 2015. Learning deep generative models. Annu. Rev. Stat. Appl. 2, 361–385. https://doi.org/10.1146/annurev-statistics-010814-020120.
Soares, A., 2001. Direct sequential simulation and cosimulation. Math. Geol. 33 (8), 911–926. https://doi.org/10.1023/A:1012246006212.
Vaswani, A., Shazeer, N., Parmar, N., et al., 2017. Attention is all you need. In: Advances in Neural Information Processing Systems 30: Proceedings of the 31st International Conference on Neural Information Processing Systems, pp. 5998–6008.
Wang, S., Xiang, J., Wang, X., et al., 2024. A deep learning based surrogate model for reservoir dynamic performance prediction. Geoenergy Sci. Eng. 233, 212516. https://doi.org/10.1016/j.geoen.2023.212516.
Wu, X., Fan, W., Peng, S., et al., 2024. Reservoir stochastic simulation based on octave convolution and multistage generative adversarial network. Sci. Rep. 14, 31618. https://doi.org/10.1038/s41598-024-80317-1.
Xie, P., Hou, J., Yin, Y., et al., 2022. Seismic inverse modeling method based on generative adversarial networks. J. Petrol. Sci. Eng. 215, 110652. https://doi.org/10.1016/j.petrol.2022.110652.
Xu, Y., Guo, L., Song, D., et al., 2025. A multiscale generative adversarial network approach for generating porous media with structural morphology. Stoch. Environ. Res. Risk Assess. 39 (9), 3957–3977. https://doi.org/10.1007/s00477-025-03044-7.
Yang, B., Wang, H.Z., Li, G.S., et al., 2022. Fundamental study and utilization on supercritical CO_2 fracturing developing unconventional resources: Current status, challenge and future perspectives. Pet. Sci. 19 (6), 2757–2780. https://doi.org/10.1016/j.petsci.2022.08.029.
Zakeri, F., Mariethoz, G., 2021. A review of geostatistical simulation models applied to satellite remote sensing: Methods and applications. Remote Sens. Environ. 259, 112381. https://doi.org/10.1016/j.rse.2021.112381.

Zhang, T., Du, Y., Li, B., et al., 2017. Stochastic reconstruction of spatial data using LLE and MPS. Stoch. Environ. Res. Risk Assess. 31 (1), 243–256. https://doi.org/10.1007/s00477-015-1197-z.

Zhang, T., Zhang, W., 2025. 3D reconstruction of digital rocks based on StyleGAN and transformer. Int. J. Coal Sci. Technol. 12 (1), 40. https://doi.org/10.1007/s40789-025-00746-9.

Zhou, X., Shi, P., 2025. Multi-scale generative adversarial network for 2D subsurface reconstruction using multi-fidelity geological exploration data. Adv. Eng. Inform. 66, 103482. https://doi.org/10.1016/j.aei.2025.103482.

Zhou, X., Shi, P., Sheil, B., 2024. Knowledge-based multiple point statistics for soil stratigraphy simulation. Tunn. Undergr. Space Technol. 143, 105475. https://doi.org/10.1016/j.tust.2023.105475.